3D Simulations of the Early Martian Hydrological Cycle Mediated by a H_2-CO_2 Greenhouse

Scott D. Guzewich, Michael Way, Igor Aleinov, Eric T. Wolf, Anthony Del Genio, Robin Wordsworth, Kostas Tsigaridis

ABSTRACT

For decades the scientific community has been trying to reconcile abundant evidence for fluvial activity on Noachian and early Hesperian Mars with the faint young Sun and reasonable constraints on ancient atmospheric pressure and composition. Recently, the investigation of H_2-CO_2 collision-induced absorption has opened up a new avenue to warm Noachian Mars. We use the ROCKE-3D global climate model to simulate plausible states of the ancient Martian climate with this absorptive warming and reasonable constraints on surface paleopressure. We find that 1.5-2 bar CO_2-dominated atmospheres with ≥3% H_2 can produce global mean surface temperatures above freezing, while also providing sufficient warming to avoid surface atmospheric CO_2 condensation at 0°-45° obliquity. Simulations conducted with both modern topography and a paleotopography, before Tharsis formed, highlight the importance of Tharsis as a cold trap for water on the planet. Additionally, we find that low obliquity (modern and 0°) is more conducive to rainfall over valley network locations than high (45°) obliquity.

1. INTRODUCTION

Abundant geologic evidence strongly implies that surface liquid water was widespread on ancient Mars approximately 3.5-4 billion years ago, in the time period termed the Noachian. Such evidence includes riverine channels (e.g., Masursky, 1973; Pieri, 1980; Hynek and Phillips, 2001; Hynek et al., 2010), craters filled with sedimentary deposits and including inflow and outflow channels (e.g., Irwin et al., 2005; Fasset and Head, 2005; Schon et al., 2012), minerals that only

form in the presence of liquid water (e.g., Murchie et al., 2009; Ehlmann et al., 2011; Carter et al., 2013), and features implying aqueous erosion (e.g., Carr, 1996; Malin and Edgett, 2000).

Work to deduce what climatic conditions were possible to produce such geologic evidence has been ongoing for decades and Wordsworth (2016) provides a recent review of the state of knowledge. One-dimensional radiative-convective models were initially used (e.g., Pollack, 1979; Pollack et al., 1987) and habitable conditions (typically defined as global mean surface temperatures above 273 K) were generated with sufficiently large surface air pressures of CO_2-dominated atmospheres, even with the ~25% dimmer young Sun, although not in all models (e.g., Postawko and Kuhn, 1986). Kasting (1991) showed that CO_2-H_2O atmospheres alone were insufficient to warm ancient Mars due to increased Rayleigh scattering at high pressure and CO_2 ice condensation on the surface. Increasing sophistication of the models (e.g., incorporation of cloud effects) over time and doubts about the plausibility of very thick (>2 bar) atmospheres made reconciling the geologic evidence challenging. A plethora of greenhouse mixtures (CH_4, NH_3, SO_2, cirrus clouds, and others) have been proposed, but all have unique problems being retained in a putative ancient atmosphere (e.g., Kuhn and Atreya, 1979; Kasting, 1997; Tian et al., 2010; Urata and Toon, 2013; Mischna et al., 2015; Kerber et al., 2015; Turbet et al. 2020a). More recently, indirect evidence (e.g., crater counting statistics) has implied that the ancient martian atmospheric pressure was likely less than 1 bar, with perhaps 2 bar being consistent with the data, at least for geologically short time periods (Cassata et al., 2012; Manga et al., 2012; Kite et al., 2014; Warren et al., 2019).

Limiting ancient martian atmospheric pressure to terrestrial-comparable levels in combination with the Faint Young Sun presents a strong challenge to long-term (i.e., tens to hundreds of millions of years) “warm and wet” conditions. More punctuated and brief warm

31 climate periods interspersed with cold and dry conditions (perhaps with seasonal melting) also
32 may fit some of the geologic evidence while also being consistent with Mars general circulation
33 models (Fastook et al., 2012; Wordsworth et al., 2013; Fastook and Head, 2015; Cassenelli and
34 Head, 2015; Wordsworth et al., 2015). Yet, some geologic evidence (e.g., Williams et al., 2013,
35 Grant et al., 2014; Grotzinger et al., 2014; Kite et al., 2017) still requires some persistent duration
36 of warm and wet conditions. Recently, H_2 has been offered as another possible greenhouse gas
37 (Wordsworth and Pierrehumbert, 2013; Ramirez et al., 2014). Importantly, collision-induced
38 absorption (CIA) between H_2 and CO_2 has been shown to be efficacious at generating considerable
39 warming through *ab initio* calculations (Wordsworth et al., 2017) and experiments (Turbet et al.,
40 2019, 2020; Godin et al., 2020; Mondelain et al., 2021), although the experimental results
41 demonstrate slightly more modest absorption than the *ab initio* calculations.
42 One-dimensional climate models including CIA between H_2, CO_2, and CH_4 generate global
43 mean surface temperatures above the freezing point of water for reasonable atmospheric pressures
44 during the Noachian period (Ramirez et al., 2014; Batalha et al., 2015; Wordsworth et al., 2017;
45 Hayworth et al., 2020). Three-dimensional general circulation models (GCMs) have also begun
46 experiments including such CIA absorption (Haberle et al., 2019; Kamada et al., 2020). One
47 challenge that remains however, is retaining comparatively large partial pressures of H_2, which
48 should have escaped rapidly during a time period when the Sun was more active (e.g., Jakosky et
49 al., 2018). Ramirez et al. (2014) suggested the martian mantle may be more reduced and thus emit
50 more H_2 relative to Earth, while still producing CO_2 through chemical processes in the atmosphere
51 (see Hirschmann and Withers (2008) which imply reduced CO_2 outgassing from a reduced mantle).
52 Water-rock chemical reactions (particularly with iron-bearing materials) could have generated
53 substantial H_2 fluxes (Hurowitz et al., 2010; Tarnas et al., 2018; Tosca et al., 2018). Haberle et al.

(2019) suggests that iron-rich meteorites impacting Mars would have degassed abundant H_2, creating large H_2 partial pressures for short durations (up to 10^4 years for 100 km sized objects) following the impact.

In this work, we examine two science questions related to the early martian climate:

1. What range of atmospheric pressure and greenhouse gas mixtures can permit global mean annual surface temperatures above the freezing point of water?
2. What is the fate of liquid water on the surface of ancient Mars?

We have performed a range of GCM simulations with the Resolving Orbital and Climate Keys of Earth and Extraterrestrial Environments with Dynamics 1.0 (ROCKE-3D) general circulation model to study these questions. Our radiative transfer model employs the CIA absorption as described by Wordsworth et al. (2017) and is flexible enough to allow varying surface pressures, gas mixtures, and global water inventories. In Section 2 we describe our methodologies and the radiative transfer scheme in detail. In Section 3 we present and discuss our results. Finally, in Section 4 we conclude.

2. METHODOLOGY

We employ the ROCKE-3D GCM for our simulations. Way et al. (2017) describes the broad capabilities of ROCKE-3D to simulate rocky planet atmospheres both in and out of the Solar System. Within the Solar System, ROCKE-3D has been used to study possible paleo-environments of early Venus (Way et al., 2016; Way and Del Genio, 2020) and transient atmospheres on Earth's moon (Aleinov et al., 2019). ROCKE-3D is freely available for download at https://simplex.giss.nasa.gov/gcm/ROCKE-3D/ and instructions for setup and testing are provided.

ROCKE-3D has heritage from the NASA Goddard Institute for Space Studies ModelE2 and employs many facets of that terrestrial climate model, including the dynamical core and many physical parameterizations (e.g., water ice cloud physics, surface and subsurface runoff, ocean dynamics, etc.). As a GCM designed to simulate hypothetical exoplanet environments and ancient conditions in our Solar System, several modifications were required in the transition from ModelE2 to ROCKE-3D. First among these is the adoption of the Suite of Community Radiative Transfer codes (SOCRATES) radiation scheme [e.g., Amundsen et al., 2016] that is adaptable to non-terrestrial gas mixtures, varying stellar insolation, and stellar type. SOCRATES uses a two-stream radiative transfer solver with correlated-k distributions to solve for shortwave and longwave absorption and scattering [Edwards 1996; Edwards and Slingo, 1996]. SOCRATES can be flexibly configured to suit particular atmospheric gas mixtures, stellar spectrum, and spectral resolutions. Here, SOCRATES has been configured specifically for paleo Mars atmospheres, suitable for multi-bar CO_2 dominated atmospheres, along with H_2O, CH_4, H_2, and N_2 at lesser amounts. Gas absorption is included via the current best practices. CO_2 line absorption is included with a sub-Lorentizian line shape truncated at 500 cm^{-1} from the line centers. H_2O and CH_4 line absorption assumes a Voigt profile truncated at 25 cm^{-1} from the line centers. The H_2O self and foreign broadened continua are included using the MT_CKD version 3.0 continuum model (Clough et al. 2005), and collision induced absorption (CIA) for CO_2-CO_2 and other important pairs are also included.

Figure 1 shows the input stellar spectrum used in this work, taken as the Sun spectrum at 3.8 Ga from Claire et al. (2012) with the spectral scaling calibrated to Lean et al. (1995), and with the total solar flux scaled to Mars at this time period (442 Wm^{-2}). Our Sun has slowly brightened over time (Gough, 1981), and at 3.8 Ga the Sun was only ~75% as luminous as it is today. Also,

at this time period, the Sun was slightly redder, with an effective temperature of about ~100 K cooler than it is today (Claire et al., 2012). The result of the effective temperature change is that slightly more radiation is emitted in the near-infrared compared to the visible, relative to the present-day Sun. In practice, assuming an identical incident stellar flux, the downwelling stellar flux that reaches the surface through a nominal early Mars-like atmosphere is lessened by only a few tenths of Wm^{-2} compared to the using the present-day Sun spectrum. Overlaid on Figure 1 are the 46 shortwave bands used in our model. Previous works have shown that adequate shortwave radiative transfer performance requires resolving absorption bands and windows in the near-infrared (Yang et al. 2016). Thus, 46 bands were used to parse out H_2O, CO_2, and CH_4 absorption in this spectral region.

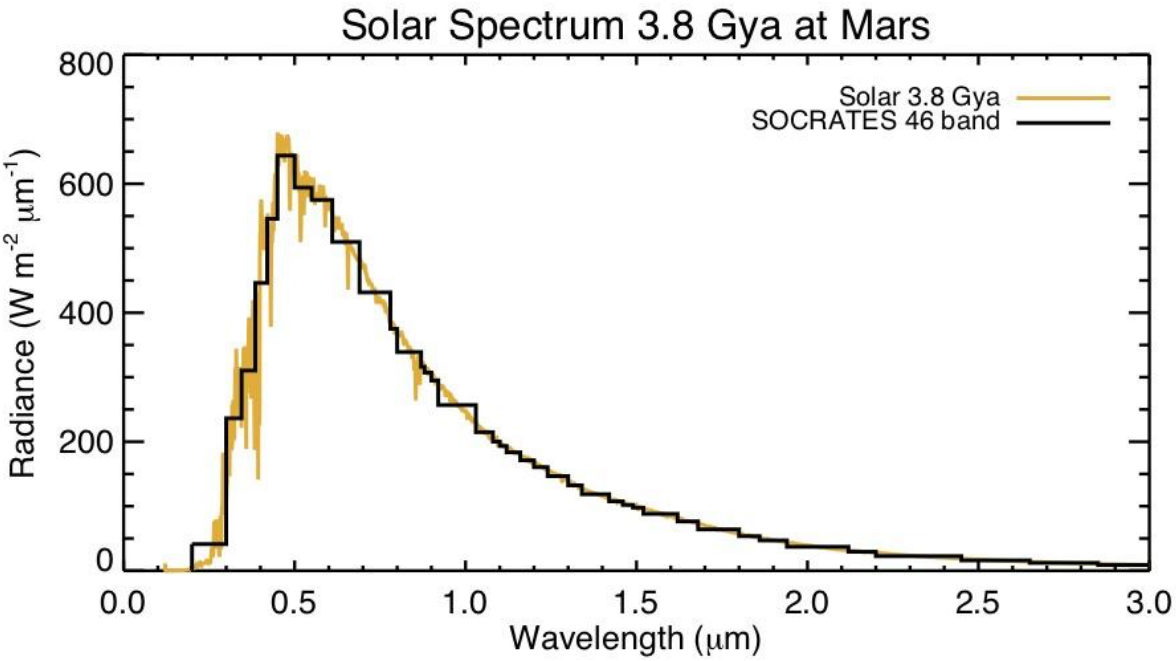

Figure 1: The stellar spectrum at 3.8 Ga (orange) along with the 46-band discretization of this stellar spectrum used in our SOCRATES shortwave radiative transfer calculation (black).

Figure 2 illustrates the longwave performance of our radiative transfer model. Here, duplicating previously published calculations, we assume a 2-bar pure CO_2 atmosphere with a 250 K surface temperature, a dry adiabatic lapse rate, and a 167 K isothermal stratosphere. We compare radiative transfer calculations from SOCRATES using the GCM resolution (16 bands), a high-resolution configuration of SOCRATES (350 bands), and also with published calculations using SMART (see Kopparapu et al. 2013, Fig. 1). Our SOCRATES calculations, both with the GCM resolution and high-resolution versions, underestimate CO_2 absorption thus allowing more outgoing longwave radiation (OLR) by ~8 Wm^{-2} compared with SMART calculations at 88.5 Wm^{-2}. Identical calculations conducted by Wordsworth et al. (2010) using a two-stream correlated-k approach indicate an OLR of 88.17 Wm^{-2}. However, more recent calculations featured in Wordsworth et al. (2017, supplemental materials), that used a line-by-line multi-stream approach, yielded an OLR of ~92 Wm^{-2}. By either comparison, our model features somewhat weaker thermal absorption by CO_2 compared with other published results, meaning that our pure-CO_2 simulations may yield slightly colder surface temperatures than other codes.

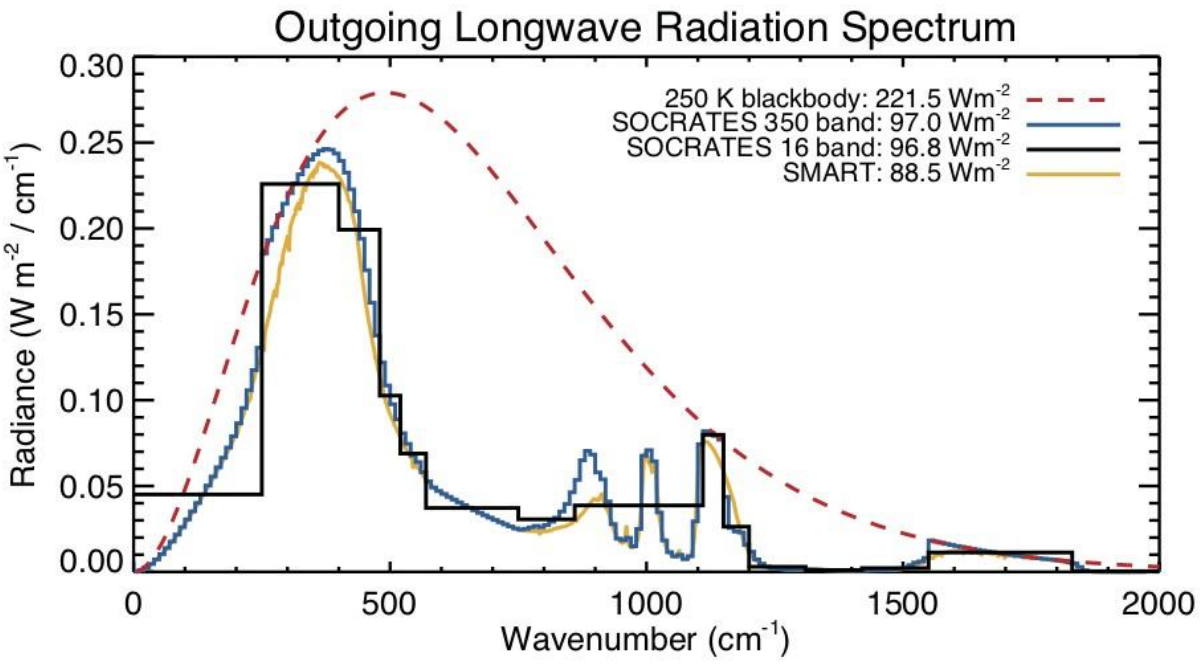

Figure 2: Outgoing longwave radiation spectrum from a 250 K blackbody (red dashed) and from 1-D offline radiative transfer calculations using SOCRATES at high resolution (blue), the GCM resolution (black), and SMART (orange). Here we have assumed a 2-bar CO_2-only atmosphere with a 250 K surface temperature and 167 K isothermal stratosphere. Our model underestimates absorption by a pure-CO_2 atmosphere.

Note, that here we have used the ab initio CO_2-H_2 and CO_2-CH_4 CIA from Wordsworth et al. (2017). However, recent laboratory work by Turbet et al. (2020b) argues that the Wordsworth CIA's overestimate their greenhouse effect. Further note that Godin et al. (2020) independently conducted laboratory measurements of CO_2-H_2 and CO_2-CH_4 CIAs which are in agreement with those measured by Turbet et al. (2020). To test potential biases, here we have performed off-line calculations with SOCRATES to assess the differences between the Wordsworth et al. (2017) and Turbet et al. (2020b) CIA's. Assuming an atmospheric composition of 90% CO_2, 2% CH_4 or H_2, and N_2 constituting the remainder in a 2-bar atmosphere, we have found that the Wordsworth et al. (2017) CIA's overestimate longwave absorption by ~3 and ~8 Wm^{-2} compared to the Turbet et al. (2020b) for CO_2-CH_4 and CO_2-H_2 CIA's respectively. Thus, fortuitously, our model benefits from the cancellation of errors, between an underestimation of absorption by pure CO_2, and an overestimation of absorption by the Wordsworth et al. (2017) CIA's compared to the new laboratory measurements.

The surface hydrological cycle is represented by a system of dynamic lakes and a groundwater scheme. The lakes are assumed to have a conical shape, so they change their exposed area depending on the amount of stored water. If the amount of stored water exceeds a pre-defined sill depth, the excess of water is moved to the lake system in a neighbouring cell according to a

prescribed river routing scheme. If no river routing is prescribed for a particular cell, the lake is allowed to grow there indefinitely. The ground hydrology part employs a six-layer soil scheme (Abramopoulos et al., 1988; Rosenzweig & Abramopoulos, 1997) with the upper layer being 0.1 m deep and the rest growing geometrically with depth up to a total of 3.5 m. The thermal and hydrological properties of each layer are computed according to the prescribed composition of soil components (sand, clay, silt) and present water. The heat between the layers is exchanged according to the thermal conductivity law and can be transported by water. The water can drain to the lower layers due to gravity (according to Darcy's law) or it can be taken to the upper layers by the capillary uplifting. The amount of water in each layer is not allowed to exceed the saturation level or fall below the hygroscopic minimum, which are defined by the local soil texture. The bottom of the lowest layer is assumed to be impermeable to heat and water. Part of the water from each layer can be lost to underground runoff, which is assumed to be proportional to the local slope (prescribed according to the local topography). The upper soil layer can also experience surface runoff, which depends on its level of saturation and the strength of the rain storm. All runoff water is redirected to the local lakes. All heat and water exchange with the atmosphere is performed through the upper layer. The upper layer of soil receives water from precipitation and condensation and loses it through evaporation and runoff. If the precipitation is in a solid form, the ground hydrology algorithm forms a snowpack. The snowpack is represented by a three-layer snow model with its own melting and refreezing cycle. The fraction of the ground covered by snow is defined by the snow thickness and local topography. The lakes can also form lake ice when the amount of heat in the lake falls below the freezing threshold, and they can accumulate snow on top of the ice. The albedo of the surface is defined by the fraction of the lakes, the albedo of the bare soil (which is prescribed for the dry soil, but can decrease when the soil gets wet) and the fraction of ice and

177 the snow. The albedo of the snow depends on the grain size and is assumed to decrease with its
178 age (Hansen et al., 1983).

179 For our ancient Mars simulations discussed in this work, we run the model at 4° latitude
180 by 5° longitude resolution with 40 vertical atmospheric layers from the surface (500-2000 mb) to
181 ~0.1 mb at the top. Mars orbital parameters use modern values except for specific simulations
182 where obliquity is changed as discussed below. Similarly, we use modern Mars topography for
183 simplicity in most simulations and initialize the surface as having uniform 15% broadband albedo
184 with sandy soil. It's reasonable to assume that the Noachian surface could have been darker than
185 the modern due to less surface oxidation, although snow and ice cover could have offset that to
186 some degree. Of course the true Noachian surface albedo is unknown, but note this value of 15%
187 is lower than some other Noachian Mars climate simulations, many of which use modern surface
188 albedo distributions (e.g., Forget et al., 2013). Some simulations (detailed below) use a possible
189 paleotopography (Table 1) shown by Bouley et al. (2016) (see also Matsuyama and Manga, 2010)
190 before the development of the Tharsis Montes and associated true polar wander (TPW). All
191 simulations use an "active lakes" capability of ROCKE-3D (also used for ancient Venus by Way
192 et al., 2016) where the model can produce bodies of surface liquid water based on runoff and
193 precipitation patterns. In some simulations, we initialize the model with existing surface liquid
194 water as "lakes" in topographic low points such as Hellas Basin, deep craters, and the northern
195 lowlands. The model simulates an active water cycle with frozen and liquid precipitation,
196 deposition of snow on the surface, and surface runoff. Note the model does not include CO_2 ice
197 in the atmosphere or on the surface, even if the temperature falls below the frost point. Some
198 ancient Mars climate studies have suggested that CO_2 ice clouds may play an important role in
199 warming the planet's surface (Forget and Pierrehumbert, 1997; Forget et al., 2013; Wordsworth et

al., 2013). CO_2 cloud physics are in development for ROCKE-3D and their impacts will be examined in future work.

Our simulations are all run until they reach radiative equilibrium. Simulations that are initialized with "dry" soil (and thus have minimal, but nonzero, global water inventory) are run for 20 Mars years with the final year used for results below. Simulations initialized with "wet" soil or with surface liquid water are run until they both reach radiative and hydrological equilibrium. Evaluating hydrological equilibrium is discussed below. In practice, hydrological equilibrium requires ~500 Mars years of model run time with modern topography and 2000 years or more for the paleotopography.

All our simulations are listed in Table 1. Any gas mixtures that do not sum to 100% include the remaining percent as N_2. Simulations with initialized surface water are presented as the total volume (in global equivalent layer, GEL) and whether the water was initialized as lakes or oceans in the model.

Table 1.

Simulation	Surface Pressure (bar)	% CO2	% H2	% CH4	Soil Moisture	Topography	Surface Water	Obliquity
05H0	0.5	89	0	1	Dry	Modern	None	25.19°
05H3	0.5	86	3	1	Dry	Modern	None	25.19°
1H0	1	89	0	1	Dry	Modern	None	25.19°
1H3	1	86	3	1	Dry	Modern	None	25.19°
AK1	1	97	3	0	Dry	Modern	None	25.19°
RW1	1	94	5	1	Dry	Modern	None	25.19°
1H6	1	83	6	1	Dry	Modern	None	25.19°
RH1	1	90	10	0	Dry	Modern	None	25.19°
15H0	1.5	89	0	1	Dry	Modern	None	25.19°

15H3	1.5	86	3	1	Dry	Modern	None	25.19°
15H5	1.5	94	5	1	Dry	Modern	None	25.19°
AK15	1.5	97	3	0	Dry	Modern	None	25.19°
RH15	1.5	90	10	0	Dry	Modern	None	25.19°
2H0	2	89	0	1	Dry	Modern	None	25.19°
2H3	2	86	3	1	Dry	Modern	None	25.19°
AK2	2	97	3	0	Dry	Modern	None	25.19°
RW2	2	94	5	1	Dry	Modern	None	25.19°
RW2wet	2	94	5	1	Wet	Modern	None	25.19°
RH2	2	90	10	0	Dry	Modern	None	25.19°
RW2lakes	2	94	5	1	Wet	Modern	10m GEL Lakes	25.19°
RW2lakeso0	2	94	5	1	Wet	Modern	10m GEL Lakes	0°
RW2lakeso45	2	94	5	1	Wet	Modern	10m GEL Lakes	45°
RW2lakes100	2	94	5	1	Wet	Modern	100m GEL Lakes	25.19°
RW2lakes100o0	2	94	5	1	Wet	Modern	100m GEL Lakes	0°
RW2lakes500	2	94	5	1	Wet	Modern	500m GEL Lakes	25.19°
RW2TPWlakes	2	94	5	1	Wet	Paleo	10m GEL Lakes	25.19°
RW2TPWlakeso0	2	94	5	1	Wet	Paleo	10m GEL Lakes	0°
RW2TPWlakeso45	2	94	5	1	Wet	Paleo	10m GEL Lakes	45°
RW2TPWlakes100	2	94	5	1	Wet	Paleo	100m GEL Lakes	25.19°
RW2TPWlakes100o0	2	94	5	1	Wet	Paleo	100m GEL Lakes	0°

RW2TPWlakes500	2	94	5	1	Wet	Paleo	500m GEL Lakes	25.19°
NHOcean	2	94	5	1	Wet	Modern	Ocean	25.19°
HOcean	2	94	5	1	Wet	Modern	Ocean	25.19°

214

215

216 3. RESULTS

217 We group our simulations into two categories: those initiated with no surface liquid water
218 and either dry or wet soil and those initiated with some inventory of surface liquid water. We use
219 the first group, which we generally term as "dry" simulations, to find gas mixtures and surface
220 pressure values that are supportive of surface liquid water to use in the "wet" simulations (those
221 initiated with surface liquid water).

222 3.1. Dry Simulations

223 Our dry simulations all use surface pressures between 0.5 and 2 bar at intervals of 500 mb
224 with a variety of gas mixtures. All simulated atmospheres have 83-94% CO_2, 0-6% H_2, 1% CH_4,
225 and any remainder to reach 100% is N_2 (with the exception of the simulations detailed below that
226 use gas mixtures described in the literature). H_2O is treated as a trace gas in all simulations and
227 is not assumed to ever make a substantive change to the mean molecular weight of the
228 atmosphere. In most of our "dry" simulations, the atmosphere has no water vapor at the beginning
229 of the simulation and there is a small amount of soil moisture. In a small subset of these
230 simulations, there is a larger amount of initialized soil moisture.

231 We also conducted a series of simulations with gas mixtures and pressures described in
232 the literature. Specifically, we simulate some of the gas mixtures and pressures of Wordsworth
233 et al. (2017), Kamada et al. (2020), and Haberle et al. (2019). Wordsworth et al. (2017) used
234 94% CO_2, 5% H_2, and 1% CH_4 with surface pressures of 1 or 2 bar. Kamada et al. (2020) used
235 97% CO_2 and 3% H_2 (among others, but found some amount of seasonal melting began at that

point) and we simulated that gas mixture with surface pressures of 1, 1.5, and 2 bar. Haberle et al. (2019) used 90% CO_2 and 10% H_2 (again among others) and that was again simulated with surface pressures of 1, 1.5, and 2 bar.

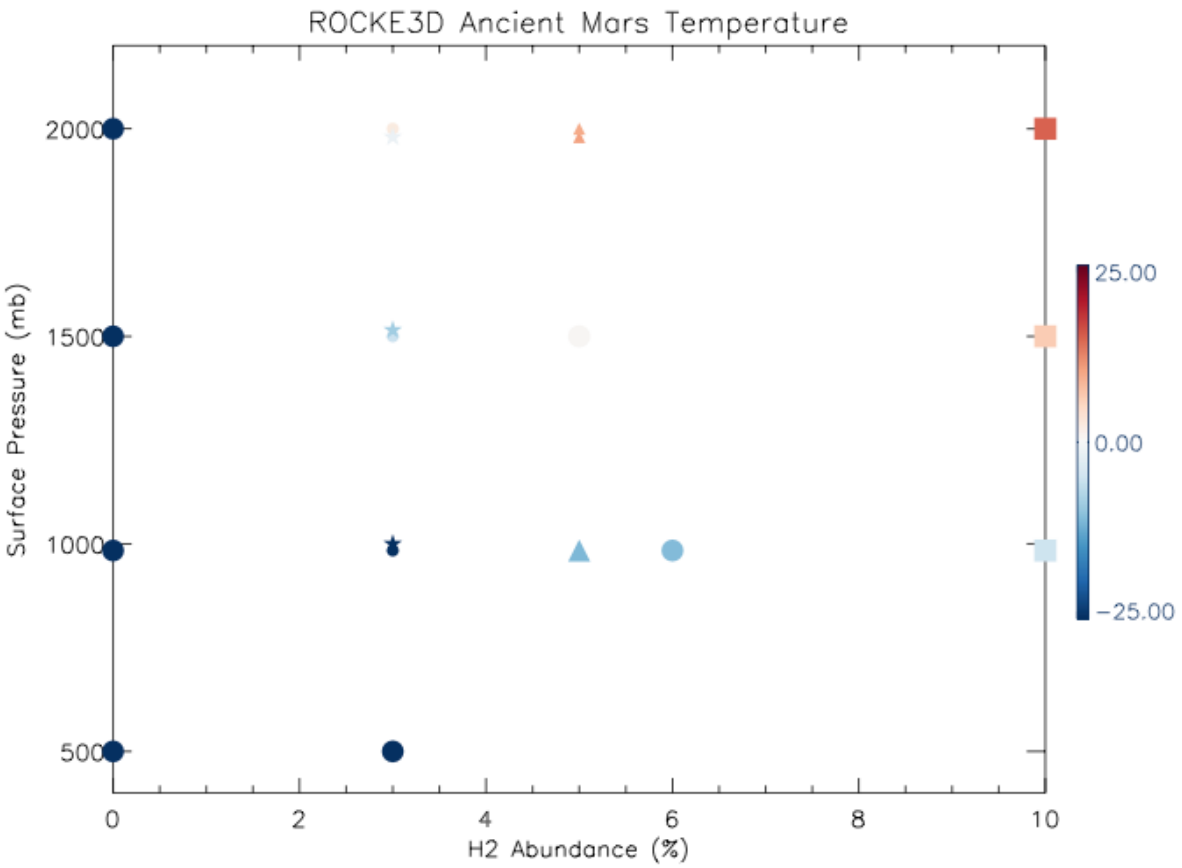

Figure 3: Global mean annual surface temperatures (°C) of "dry" ROCKE3D simulations as a function of surface pressure and H_2 abundance. Our gas mixtures are identified with circles, squares represent simulations using gas mixtures described by Haberle et al. (2019), stars represent simulations using Kamada et al. (2020) gas mixtures, and triangles represent Wordsworth et al. (2017) gas mixtures. Some simulations with similar surface pressures and H_2 abundances are indicated with smaller symbols and slightly offset in pressure for clarity.

Figure 3 shows global mean annual surface temperatures of 19 ROCKE3D simulations. A couple conclusions are immediately apparent from looking at Figure 3. First, without H_2 (and the associated CIA), even 2 bar pure CO_2 surface pressures are insufficient to produce global mean

annual surface temperatures above the freezing point of water. In fact, the 2 bar 0% H_2 simulation (Simulation 2H0 from Table 1) has a global mean annual surface temperature of -29.1°C. This is substantially warmer than a comparable atmosphere and pressure presented in Forget et al. (2013), possibly due to the lack of CO_2 condensation in ROCKE-3D which would serve to warm the middle atmosphere. Increasing H_2 abundance to 3-5% produces temperatures near freezing or slightly above freezing for Simulations 2H3, RW2, and AK2. The other immediate conclusion from Figure 3 is that 1 bar surface pressure is insufficient for global mean annual surface temperatures above freezing, even with H_2 abundances of 10% as in Simulation RH1.

Compared to the published results that we have used as guidance for some gas mixtures and pressures, we find generally good agreement. Wordsworth et al. (2017) used a line-by-line spectral code to evaluate the climate impact of their *ab initio* calculations of CIA and found that CO_2 -H_2 mixtures reached 273 K with approximately 3% H_2 for 2 bar pressures and 5% H_2 at 1.5 bar pressures. Adding CH_4 reduced the amount of H_2 necessary for above freezing conditions. As seen in Table 1, our simulations following Wordsworth et al. (2017) (RW simulations) all have 1% CH_4 and 5% H_2. The resulting global mean annual surface temperatures are quite comparable to those shown by Wordsworth et al. (2017), with Simulation RW1 having a temperature of -24.5°C, Simulation RW2 having a temperature of 14.0°C, and Simulation RW2wet (with higher initial soil moisture) having a temperature of 15.7°C. The slightly warmer temperature for wetter soil conditions is due to the higher water vapor amounts in the atmosphere. Haberle et al. (2019) found that large impacts of iron-rich meteorites could degas substantial H_2 and that mixing ratios of 10% or more produce temperatures above 273 K for 1 bar or thicker atmospheres. Our 1 bar simulation, Simulation RH1 (90% CO_2 & 10% H_2), has a global mean annual surface temperature of -13.5°C, but the simulations with thicker atmospheres, Simulations RH15 and RH2, have

temperatures of 8.5°C and 23.9°C, respectively. Our simulations following Kamada et al. (2020) are similar to their "Dry-Mars" simulations with 3% H_2 and result in temperatures quite similar to theirs, with all three simulations (Simulations AK1, AK15, and AK2) having global mean annual surface temperatures below freezing. Indeed, on balance, our simulation temperatures compare quite favorably with the "Dry-Mars" simulations by Kamada et al. (2020), even for other mixing ratios of H_2, and accounting for their higher (our lower) mixing ratios of CO_2 and our inclusion of 1% CH_4.

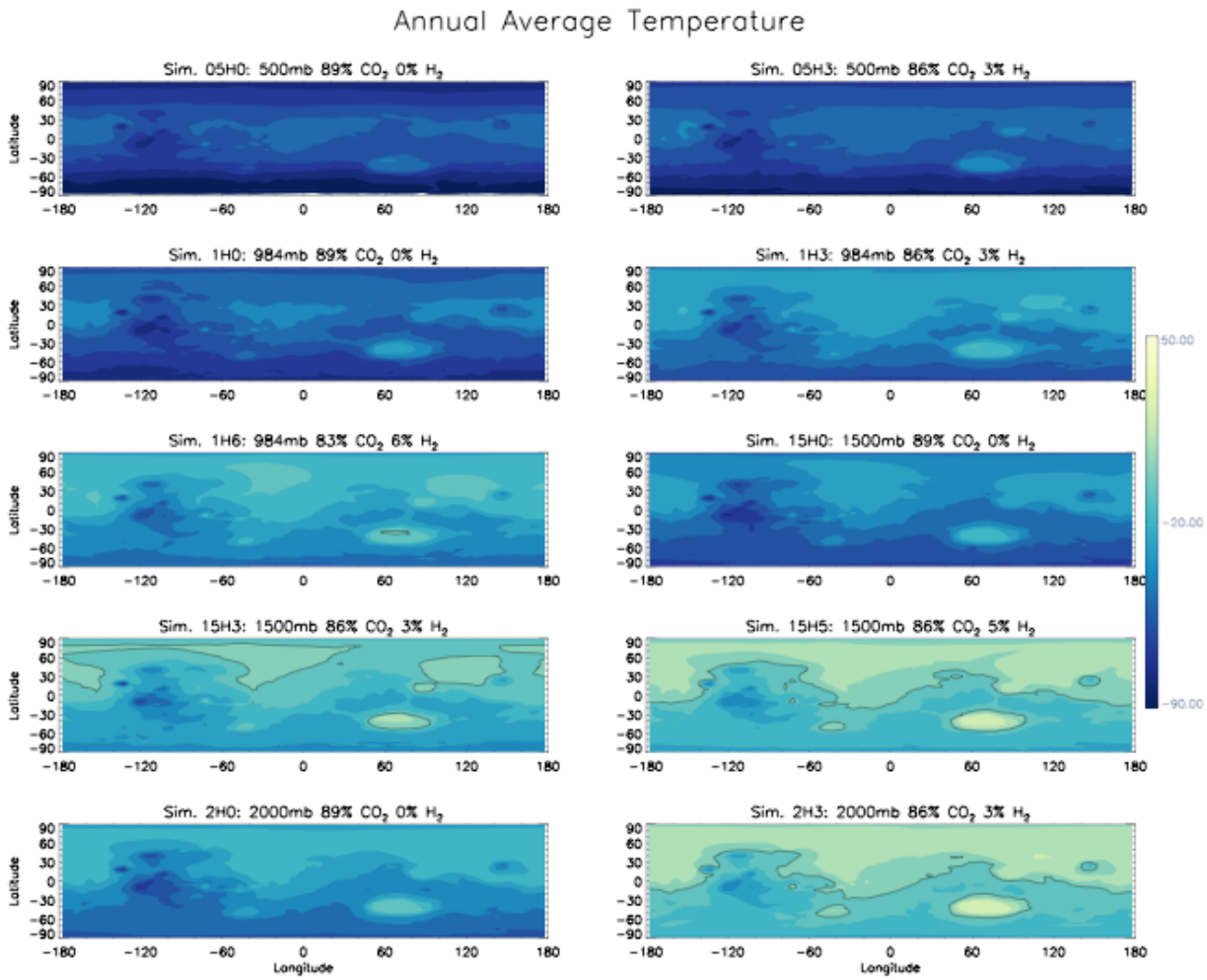

Figure 4. Mean annual surface temperatures (°C) for 10 ROCKE-3D simulations with surface pressures and CO_2 and H_2 mixing ratios identified in the panel title. All simulations incorporate dry soil. The black line indicates the freezing point of water.

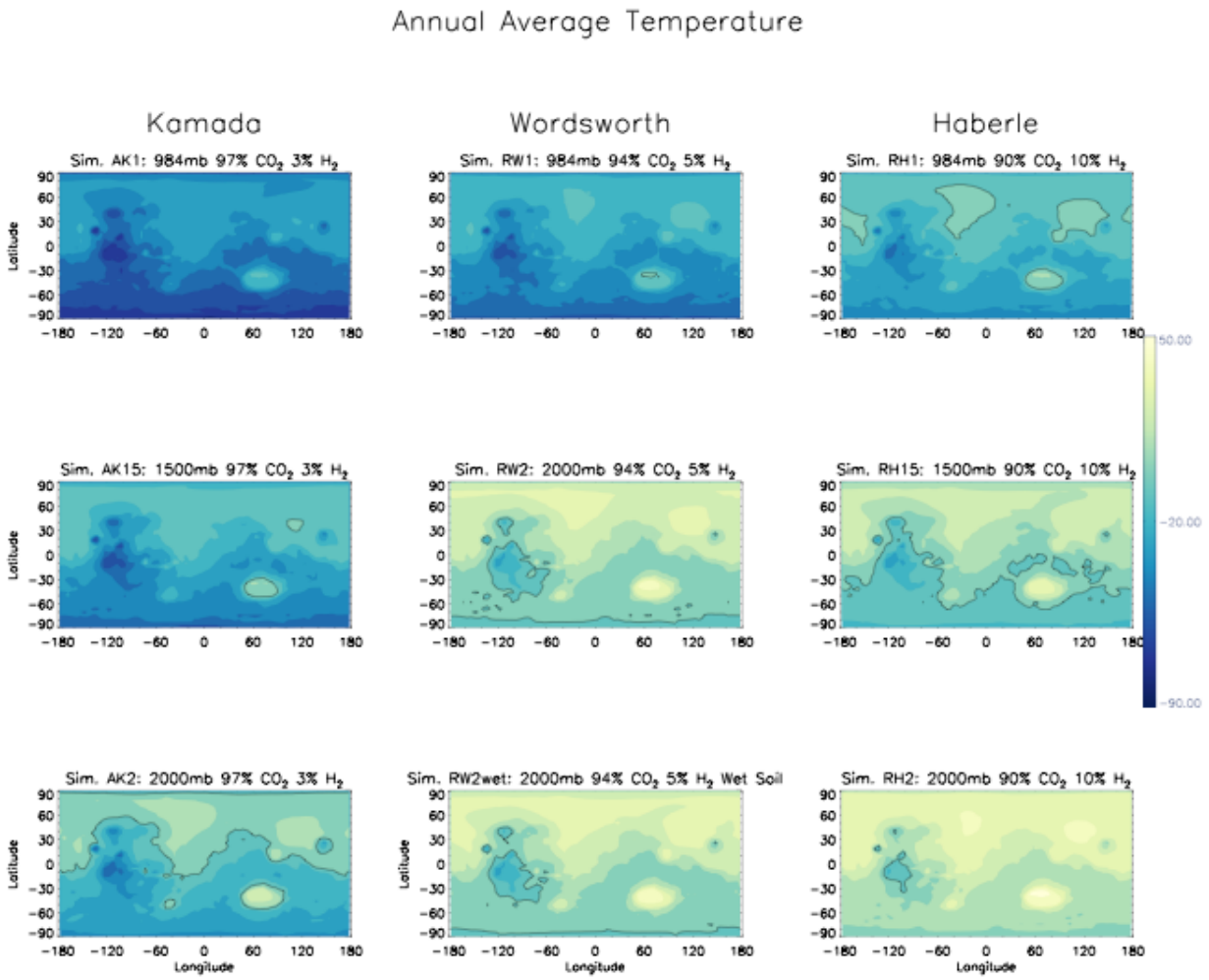

Figure 5. Same as in Figure 4, except for gas mixtures described in the literature as delineated above.

In Figures 4 and 5 we take a global view to see how temperatures vary. The same points discussed with Figure 3 generally continue to hold. Namely, even at 1 bar surface pressures, most or all of the planet sees annual average temperatures below freezing. With 5-6% H_2, small regions of Hellas Basin see above freezing annual average temperatures and increasing that to 10% H_2 in Simulation RH1 expands that to portions of the northern hemisphere lowlands. Second, some

297 amount of H_2 is necessary to have any portion of the planet experience annual average
298 temperatures above the freezing point of water. Simulation 2H0 (bottom left panel of Figure 4)
299 shows no regions of the planet above freezing despite a 2 bar atmosphere of CO_2. All planets with
300 global mean annual average temperatures above -25°C have some region of the planet above
301 freezing on an annual average basis. Simulations with increasing surface pressure and H_2 amounts
302 eventually reach a point where most of the planet is above freezing (e.g., Simulation RH2) although
303 the high elevations of the Tharsis Montes and plateau remain below freezing in all simulations.
304 This is particularly relevant for cold-trapping of water, as will be discussed below.

305 Not surprisingly, but worth mentioning, is that the regions that preferentially experience
306 above freezing annual average temperatures are the topographic lowest spots in Hellas Basin and
307 the northern lowlands. The gradient in temperatures with topography is due to adiabatic effects
308 (Wordsworth et al., 2013), which modern Mars does not experience due to its thin atmosphere.
309 These are not the locations that have the highest density of valley networks and outflow channels,
310 which fall near the topographic dichotomy boundary and in the southern hemisphere highlands
311 (Hynek et al., 2010). This disparity is well-known from studies of possible ancient martian
312 climates (e.g., Palumbo and Head, 2018).

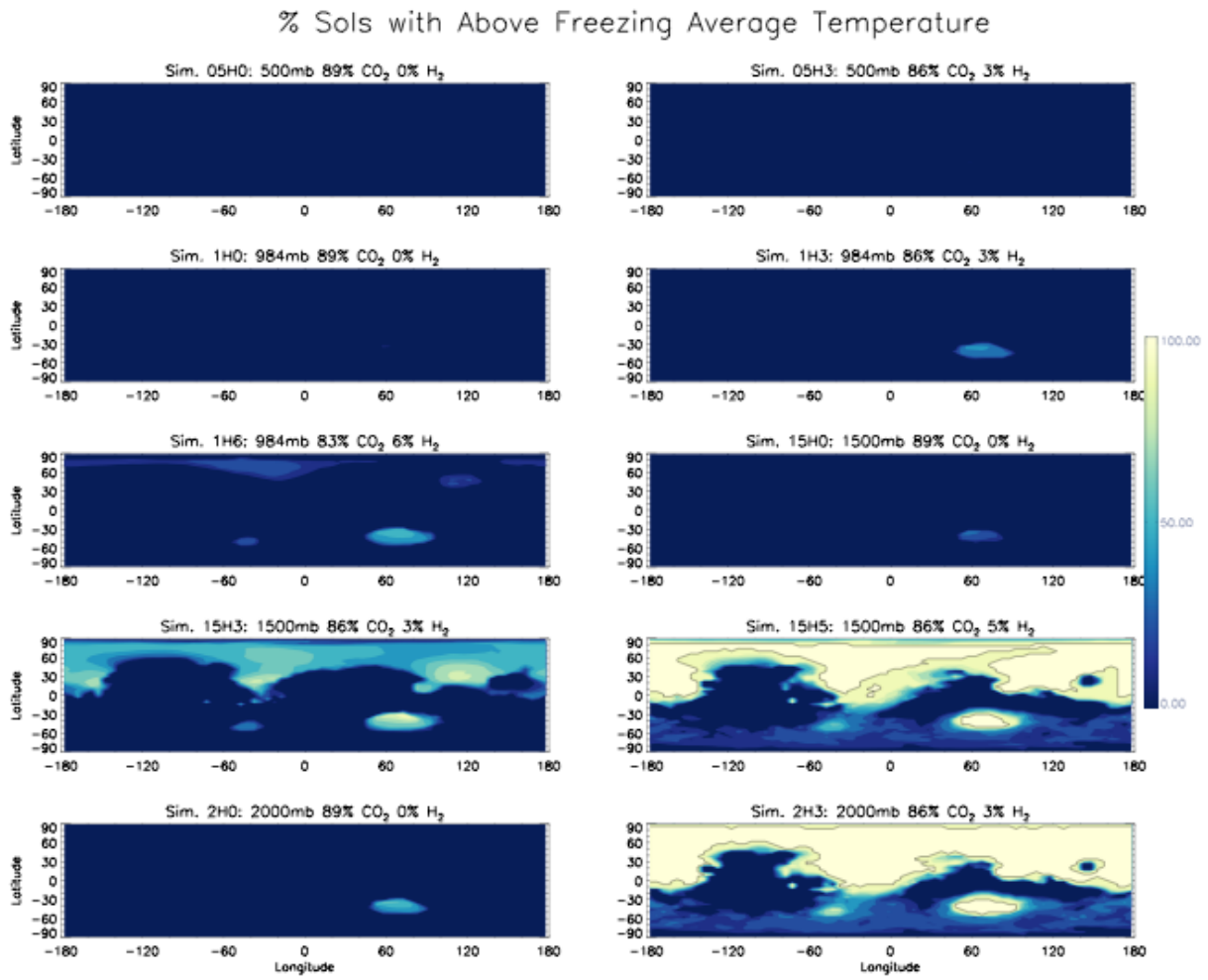

Figure 6. Percent of sols with above freezing daily average temperatures for 10 ROCKE-3D simulations with surface pressures and CO_2 and H_2 mixing ratios identified in the panel title. All simulations incorporate dry soil. The black line encloses the areas with 100%.

Looking at seasonal temperatures, we see in Figure 6 that 1 bar (with some H_2 present in the atmosphere) or higher pressure simulations all experience some regions of the planet with daily average temperatures above freezing, again predominantly in Hellas Basin or the northern lowlands. In the highest pressure and H_2 mixing ratio, and thus warmest, simulations (bottom right two panels of Figure 6) the northern lowlands and Hellas Basin are above freezing year-round. Interestingly, however, even parts of the southern hemisphere highlands (e.g., Aonia Terra and Terra Sirenum both south of the Tharsis plateau) experience seasonally warm temperatures and

some of those regions do exhibit high density of valley networks as shown by Hynek et al. (2010). That is also true of areas near the topographic dichotomy boundary in the eastern hemisphere, although the Terra Sabaea and Tyrrhena Terra regions (both with numerous valley networks) north of Hellas remain below freezing all year.

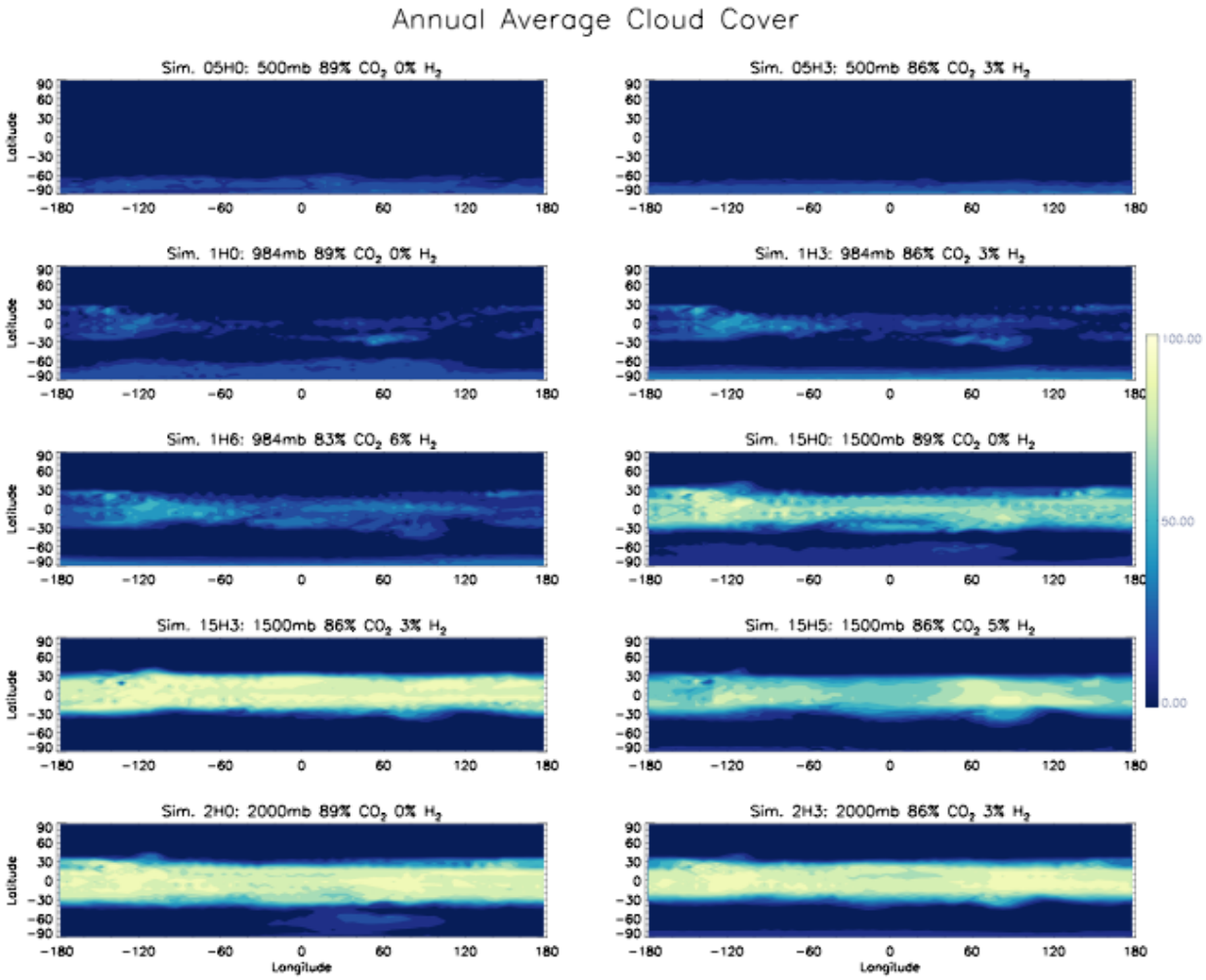

Figure 7. Annual average cloud cover for 10 ROCKE-3D simulations with surface pressures and CO_2 and H_2 mixing ratios identified in the panel title. All simulations incorporate dry soil.

As stated above, our "dry" simulations (nearly) all use initial soil moisture conditions that have a small amount of water present in the soil that is then moved through the climate system following the water cycle parameterizations in the GCM. But despite the comparatively small

338 amount of water (relative to the simulations described below in Section 3.2) in the system, the
339 simulations do produce water cloud cover. Even for modern terrestrial climate studies,
340 understanding the complete climatic influence of clouds remains an area of ongoing research and
341 much work has been done about how clouds (both H_2O and CO_2) may have impacted the ancient
342 climate of Mars (e.g., Forget et al., 2013).

343 Figure 7 shows that substantial clouds are found in the tropics. Although some convective-
344 type clouds occur over Tharsis, the bulk of the clouds are thin cirrus-like water ice clouds. The
345 coldest simulations (low pressure and lower H_2 mixing ratios) have generally clear atmospheres,
346 with infrequent tropical clouds as well as seasonal clouds over the south pole. Warmer simulations
347 (high pressure and higher H_2 mixing ratios) have a well-defined tropical cloud belt between 30°S
348 and 30°N with little longitudinal variation. Some simulations (e.g., Simulation 2H0, bottom left
349 panel of Figure 7) additionally suggest that Hellas basin sees some amount of cloud cover, which
350 is true even in the modern climate.

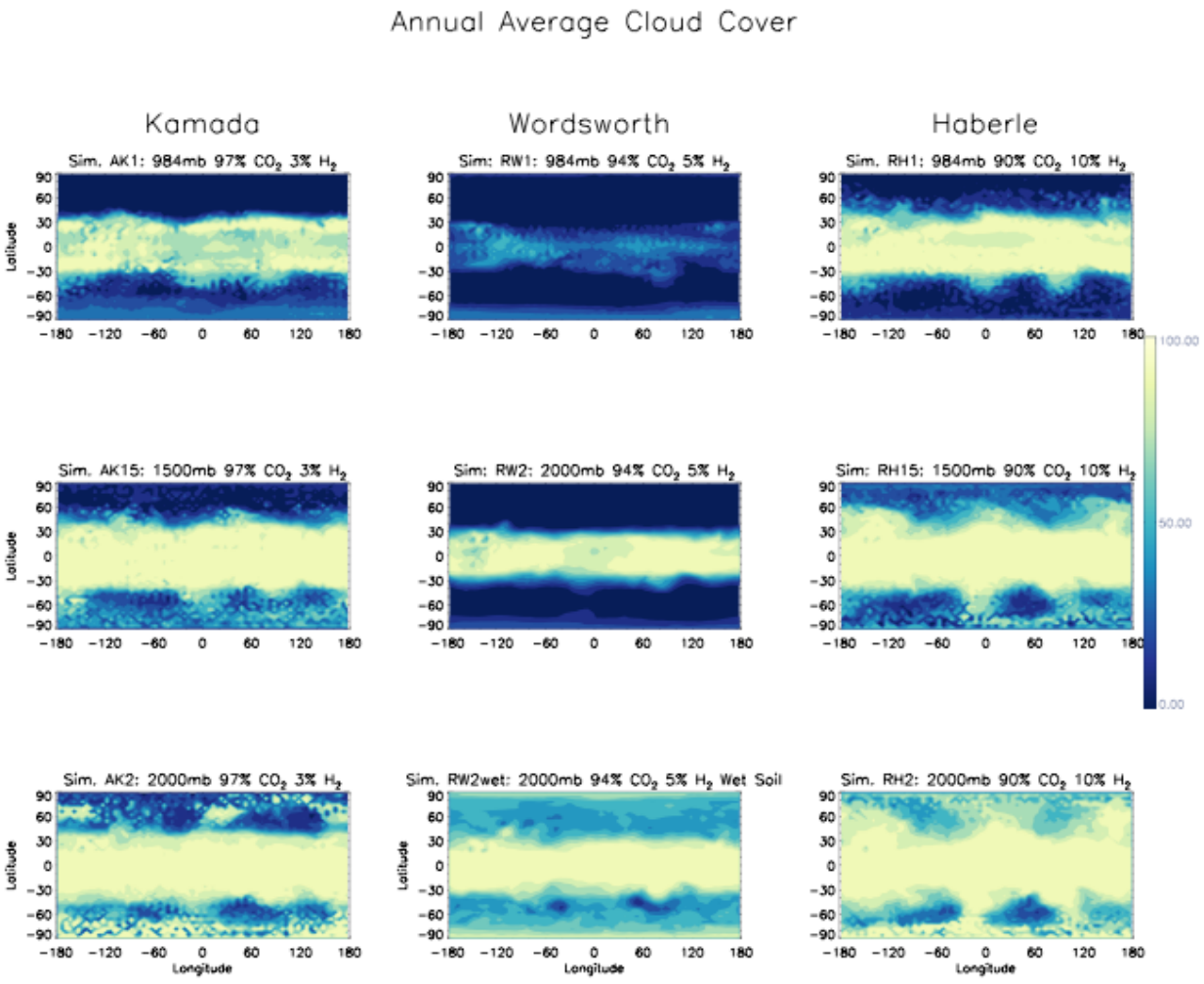

Figure 8. Same as in Figure 7, except for gas mixtures described in the literature as delineated above.

The depiction of clouds in the dry simulations is more complicated than seen in Figure 7, however, as shown in Figure 8. Whereas the 1 bar simulations in Figure 7 all have generally clear atmospheres, Figure 8 shows that Simulations AK1 and RH1 are much cloudier, more so even than the 2 bar simulations in Figure 8. In all cases (Figures 7 and 8), the clouds depicted are thin cirrus-like water ice clouds and have peak ice mixing ratios in the 100-200 mb pressure levels (see also Figure 9). Despite their broad coverage, they have minimal net radiative effect (~O(1) W/m^2).

That pattern of the Kamada and Haberle simulations being both much cloudier than the Wordsworth simulations and those in Figure 7, even when adding in a wetter soil moisture initial condition (Simulation RW2wet, bottom center panel of Figure 8), continues at higher pressures as well. The reason is ultimately their disparate atmospheric gas compositions. All simulations in Figure 7 and the Wordsworth simulations in Figure 8 all include 1% CH_4. As shown by Bryne and Goldblatt (2015) for the Archean Earth, 0.1% CH_4 and higher mixing ratios facilitate strong shortwave absorption in the troposphere and stratosphere. Wordsworth et al. (2017) also saw this higher altitude warming from CH_4. This stronger shortwave absorption is reflected in the most recent updates of the HITRAN database that ROCKE-3D uses (e.g., Rothman et al., 2013; Brown et al., 2013), but was not reflected in earlier versions. Higher CH_4 mixing ratios produce sufficient absorption to create a distinct tropopause, and this is precisely what we see when looking at our simulations (Figure 9). Despite higher specific humidities in the Wordsworth simulations and those in Figure 7, the warmer upper troposphere temperature and reduced tropospheric relative humidity limits the cloud production (see Figure 9), relative to the Kamada (AK1) and Haberle (RH1) simulations without CH_4. Increased static stability limiting cloud production in our simulations with CH_4 is analogous to similar studies of Archean Earth that removed O_2 and O_3 and noted this resulted in decreased cloud production (e.g., Wolf and Toon, 2013).

From the perspective of these simulations, the difference in cloud cover is ultimately due to warmer upper tropospheric temperatures. In all variables relevant to cloud production, the simulations without CH_4 are distinct from simulations with it (Figure 9). Simulations AK1 and RH1, without CH_4, exhibit cooler upper tropospheric temperatures and produce both thicker and more widespread cloud cover. Despite the simulations with CH_4 having a distinct tropopause, the temperature inversion is weak and water is not substantially cold-trapped. Indeed, specific

humidity values only slightly reflect the temperature inversion in the simulations with CH_4 (Figure 9). This "leaky" tropopause is similar to that on Titan, where CH_4 still mixes into the stratosphere and mesosphere and is eventually photodissociated and destroyed (e.g., Roe, 2012). Indeed, a hygropause is more efficiently produced by the thick cloud cover preventing vertical water transport (see Simulation AK1 in Figure 9). Water ice clouds also limit vertical water transport in the modern martian climate system (Clancy et al., 1996; Navarro et al., 2014). This result suggests that comparatively subtle features such as trace gas mixing ratios (i.e., CH_4 in this case) and cloud cover may have been important for water loss in the early martian climate system.

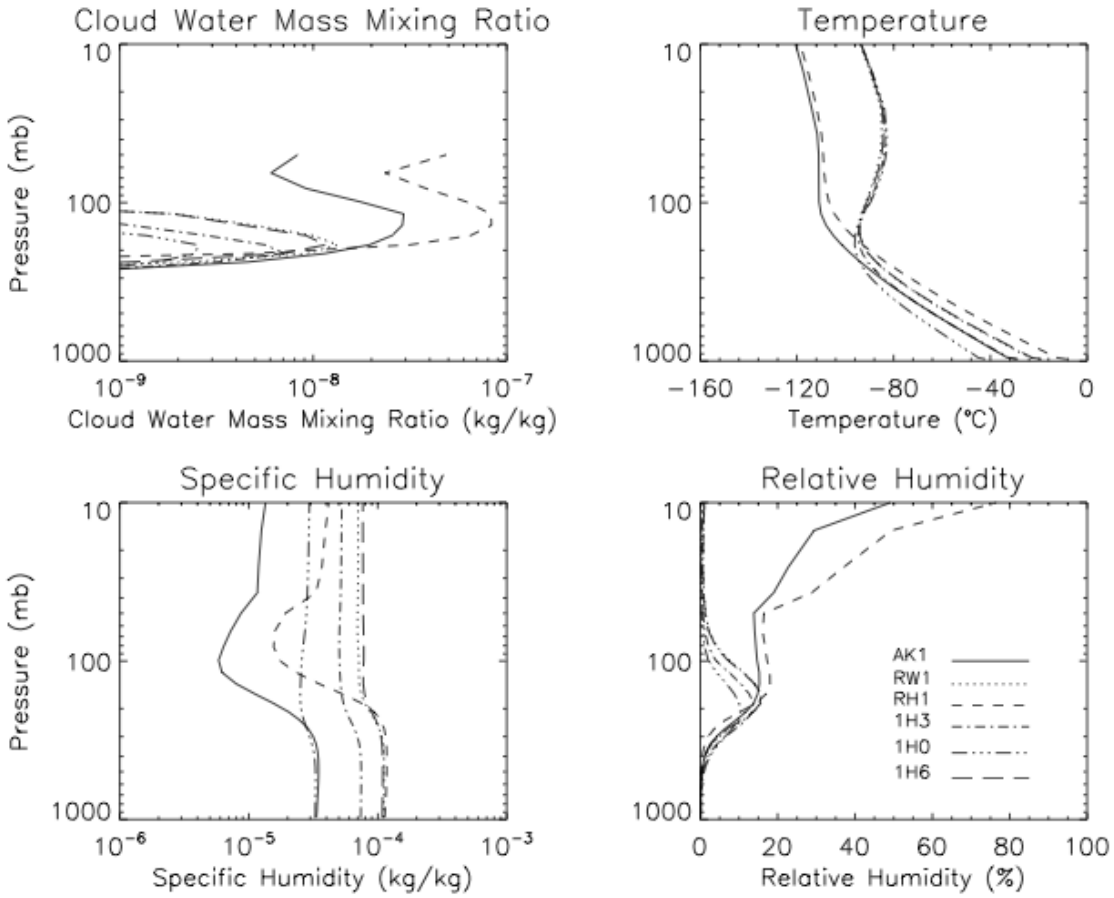

Figure 9. Average vertical profiles of cloud mass mixing ratio, temperature, specific humidity, and relative humidity for the 30°S-30°N latitude band for 6 ROCKE-3D simulations (as identified in the relative humidity panel).

3.1. Wet Simulations

Our next set of simulations are initialized with surface liquid water in the form of active lakes. Those lakes are then depleted or replenished based on the precipitation and evaporation patterns within the simulation. The first set of these "wet" simulations uses the RW2 simulation gas mixture (94% CO_2, 5% H_2 & 1% CH_4) and modern topography. Each simulation is run until hydrologic equilibrium is reached, which always takes much longer than radiative equilibrium. We define hydrologic equilibrium as the point where hydrologic variables (e.g., mass of water in lakes, mass of ground water, mass of ground ice, snow depth, and ocean ice fraction) are in steady-state.

Using modern topography, hydrologic equilibrium is always reached with all lakes on the planet being completely depleted and the remaining water in the climate system consisting of surface and subsurface snow and ice and ground water. This is due to the cold trapping of nearly all the planet's water on Tharsis, and to a lesser degree, the south pole. Wordsworth et al. [2015] also describe this cold-trapping at Tharsis and the poles with modern topography (see also Palumbo and Head [2018]). The annual precipitation patterns for this first set of six simulations is shown in Figure 10. The heaviest precipitation consistently falls on the upwind (westward) side of Tharsis, particularly Arsia Mons, for every simulation except those with 0° obliquity. In fact, the maximum annual precipitation (707 mm) occurs in the RW2lakes simulation (upper left panel of Figure 10), with only 10 m of GEL water.

In simulations with modern obliquity or 45° obliquity, there is a prominent rain shadow east of Tharsis (see also Wordsworth et al. (2015)). Comparing with Figure 11, which only shows liquid precipitation, indicates that much of the precipitation that falls over Tharsis and the south

pole falls as snow. However, the simulations with 0° obliquity are distinctly different (middle two panels of Figure 10 and 11). Simulations with 0° obliquity show much more widespread precipitation, with precipitation on both sides of Tharsis, across the topographic dichotomy boundary and through the southern highlands. Maximum precipitation at a given location (also in Tharsis) is somewhat less, however, at ~500 mm per year. Notably, the simulations with 0° obliquity have much more *liquid* precipitation than those with 25° or 45° and it is fairly evenly distributed across the low and middle latitudes including across locations with valley network formations [Hynek et al., 2010].

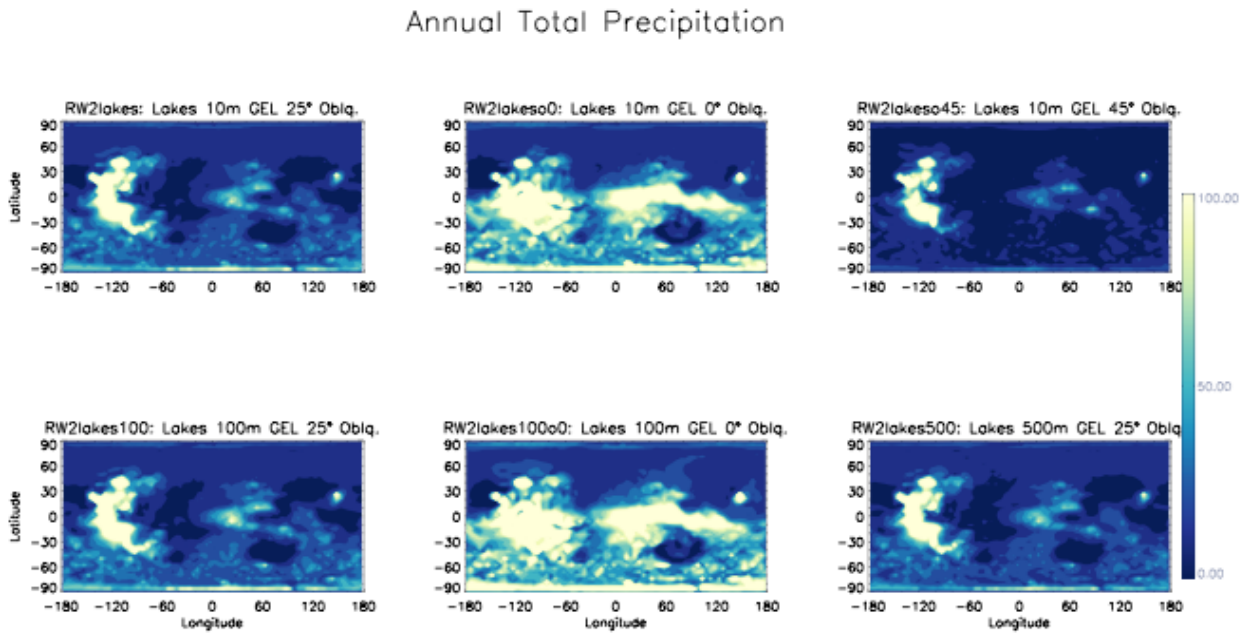

Figure 10. Annual total precipitation (mm) for 6 ROCKE-3D simulations distinguished by total initial water inventory and obliquity. All water is initialized in lakes and then moved through the climate system.

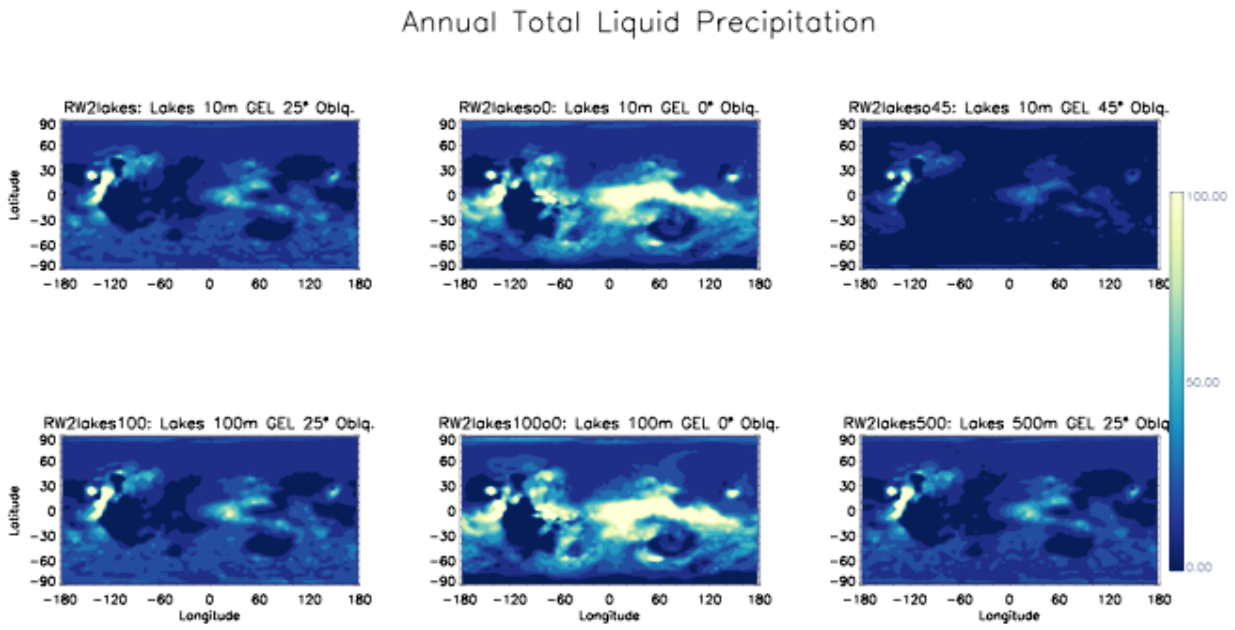

Figure 11. Same as Figure 10 except for annual total liquid precipitation (mm).

Simulations with modern or 45° obliquity show little precipitation in areas with valley network formations, regardless of the planet's initial water inventory. In fact, simulations with 45° obliquity (often suggested to be a "warmer" climate state in the literature [Palumbo and Head, 2018]) is the driest simulation over the southern highlands where valley networks are seen. Again there is minimal change to precipitation in the 0° obliquity simulations based on initial water inventory, but there is a slight increase with 100m GEL (bottom middle panel of Figures 10 and 11) relative to the 10m GEL simulation (top middle panel of Figures 10 and 11).

0° obliquity during martian history has not been thoroughly explored in the literature, particularly using three-dimensional GCMs. This is perhaps due to the expected collapse of a CO_2-dominated atmosphere into polar ice caps. Note, this version of ROCKE-3D does not have CO_2 condensation physics, as mentioned above, but mean annual temperatures in this simulation are well above the CO_2 frost point at all locations on the surface and the obliquity drives minimal seasonal variation. Our simulations show that 0° obliquity is the most plausible for producing

451 rainfall and associated runoff and erosion capable of creating the valley network formations. We
452 show this in more detail in Figure 12. We plot "monthly" (approximately 30° of solar longitude)
453 rainfall using three sample areas from Hynek et al. [2010] that have high drainage density across
454 the planet. All three locations show modest rainfall throughout the martian year. As stated above,
455 increasing the initial water inventory of the planet does not substantially alter the final hydrological
456 balance when the simulations use modern topography. Note however, that there is not perfect
457 congruence between valley network formation locations and predicted rainfall in our simulations
458 with 0° obliquity. For example, locations south of Tharsis such as the highlands of Solis Planum,
459 see near-zero rainfall in our simulations. Those locations such as Solis Planum do see snowfall
460 however, and annual average temperature there is near freezing so some seasonal melting is
461 plausible. Episodic snowmelt and runoff is another plausible formation mechanism for some
462 valley network formations (e.g., Wordsworth et al., 2015; Palumbo et al., 2020).
463

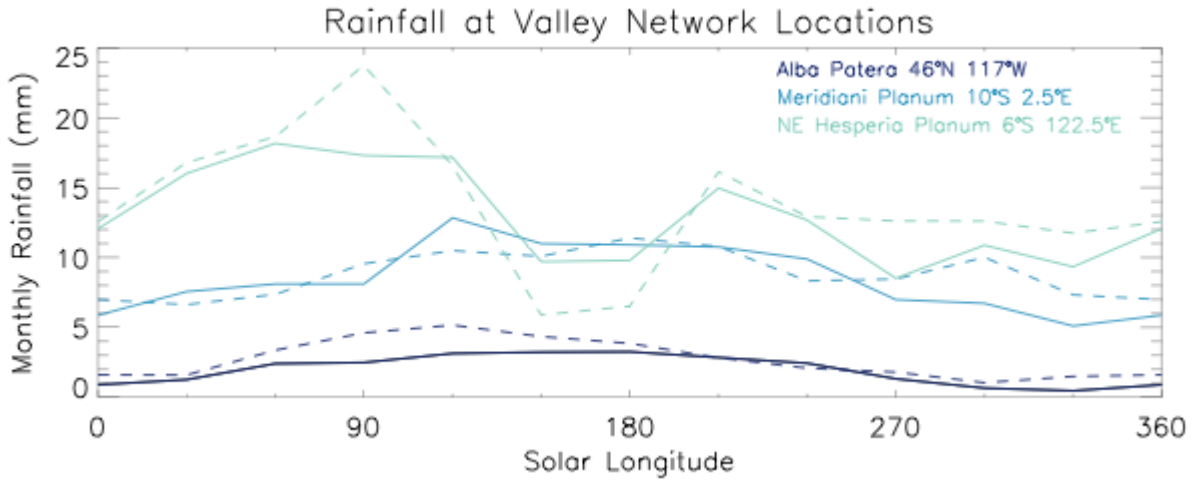

464

465 Figure 12. Simulated annual rainfall at three locations with high drainage density per Hynek et
466 al. [2010]. Solid lines indicate simulation RW2lakeso0 with 10m GEL initial water inventory and
467 dashed line indicates simulation RW2lakes100o0 with 100m GEL initial water inventory.
468 Locations are specified in the figure.
469
470

Our second set of "wet" simulations also uses the RW2 simulation gas mixture, but uses a plausible topographic map before the formation of Tharsis and associated true polar wander. We use the map from Bouley et al. (2016) (see also Matsuyama and Manga, 2010). The timing of the formation of Tharsis relative to the formation of the valley networks and lake systems on Mars is critical for understanding the plausible climate of the late Noachian. The lack of Tharsis to serve as a strong cold trap produces a much more robust hydrological cycle. Using the paleotopography, annual mean surface temperatures are comparable or slightly cooler (1-2 K) than the same simulation using modern topography (Figure 13). However, the coldest mean annual surface temperatures on the planet are ~10 K warmer in the paleotopography simulations. This is sufficient to prevent the extreme cold trapping of water that is seen on the Tharsis plateau when using modern topography. Additionally, because water is not as extensively cold trapped and more is actively circulating hydrologically, the global mean surface temperature is slightly dependent on the initial water inventory. Simulations initialized with 100 m or 500 m GEL water inventories are 5-9 K colder than equivalent simulations with 10 m GEL initial water inventory. This is due to increased snow and ice coverage and more widespread clouds in simulations with greater water inventories. Notably, the simulations with 0° obliquity are again the warmest. For example, the three simulations with 10 m GEL water inventory and obliquities of 0°, 25.19°, and 45° have global annual mean surface temperatures of: 13°C, 11.8°C, and 9.9°C, respectively.

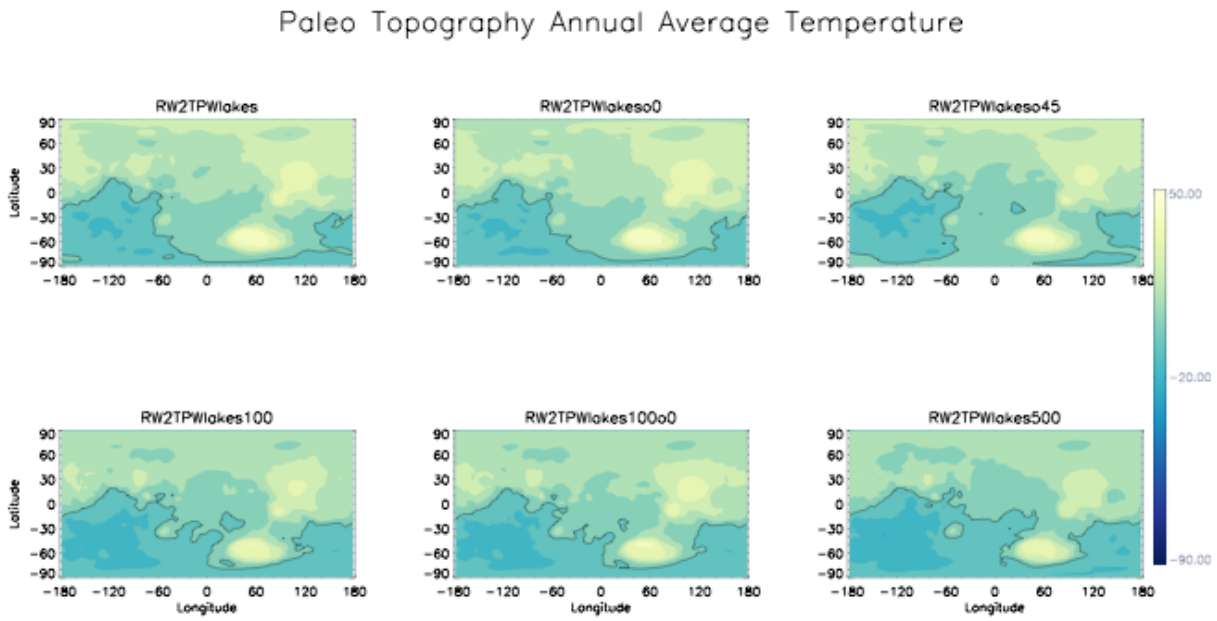

Figure 13. Mean annual surface temperatures (°C) for 6 ROCKE-3D simulations using the martian paleotopography of Bouley et al. [2016] and distinguished by total initial water inventory and obliquity. The black line indicates the freezing point of water. See Table 1 for descriptions of each simulation.

Assuming the valley networks formed prior to Tharsis formation and associated true polar wander, they would be placed in an east-west oriented band centered in the southern low latitudes near 24°S [Bouley et al., 2016]. By eye it can be seen from Figure 13 that the western portion of this band is higher (and hence colder) terrain while the center and eastern band is lower (and hence warmer) terrain. Figures 14 and 15 display annual total precipitation and annual total liquid precipitation for six simulations using the paleotopography and can be directly compared with Figures 10 and 11, which used the modern topography. However, note that the scales of those two sets of figures are different to better highlight areas of higher precipitation in the paleotopography simulations.

Simply, there is far more precipitation in simulations with paleotopography. Each simulation with paleotopography has higher maximum precipitation than the comparable simulation with modern topography. However, as can be seen by comparing Figures 14 and 15, those maxima occur as snowfall over the high terrain in the southwest hemisphere of the planet. Unlike the simulations with modern topography, precipitation increases with increasing global water inventory. Simulations with 100 m or 500 m GEL water inventories see far more precipitation in the northern hemisphere due to the more abundant surface liquid water (in the form of lakes) in the northern hemisphere lowlands in those simulations.

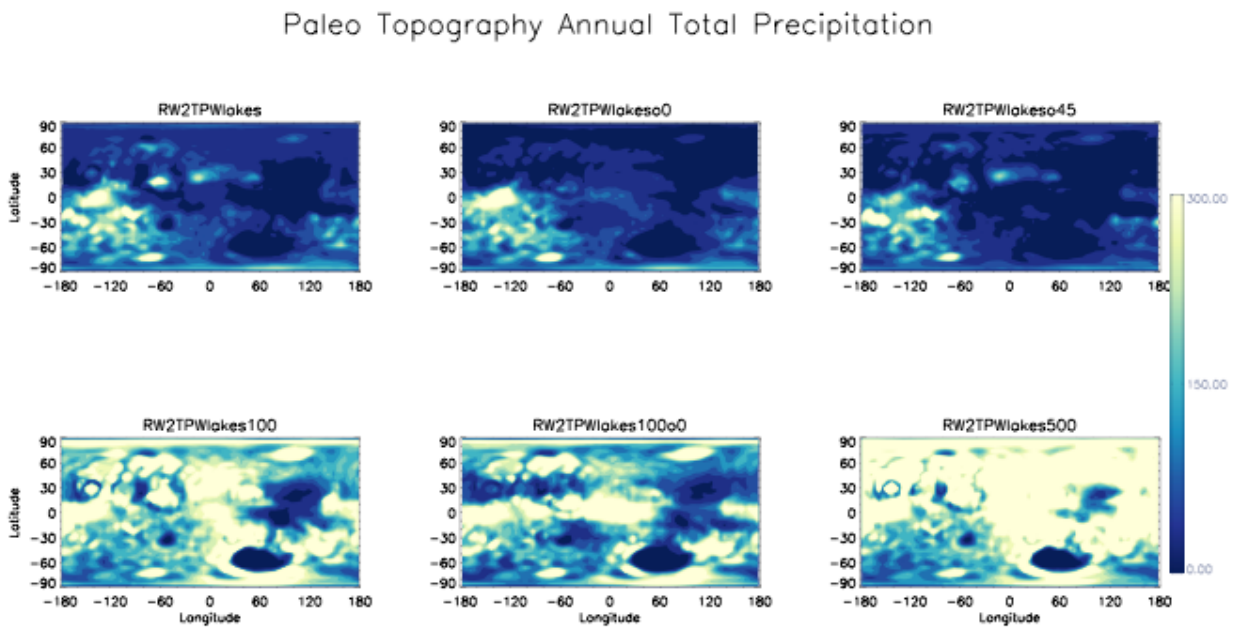

Figure 14. Annual total precipitation (mm) for 6 ROCKE-3D simulations distinguished by total initial water inventory and obliquity and using martian paleotopography. All water is initialized in lakes and then moved through the climate system. Note the different scale relative to Figure 10. See Table 1 for descriptions of each simulation.

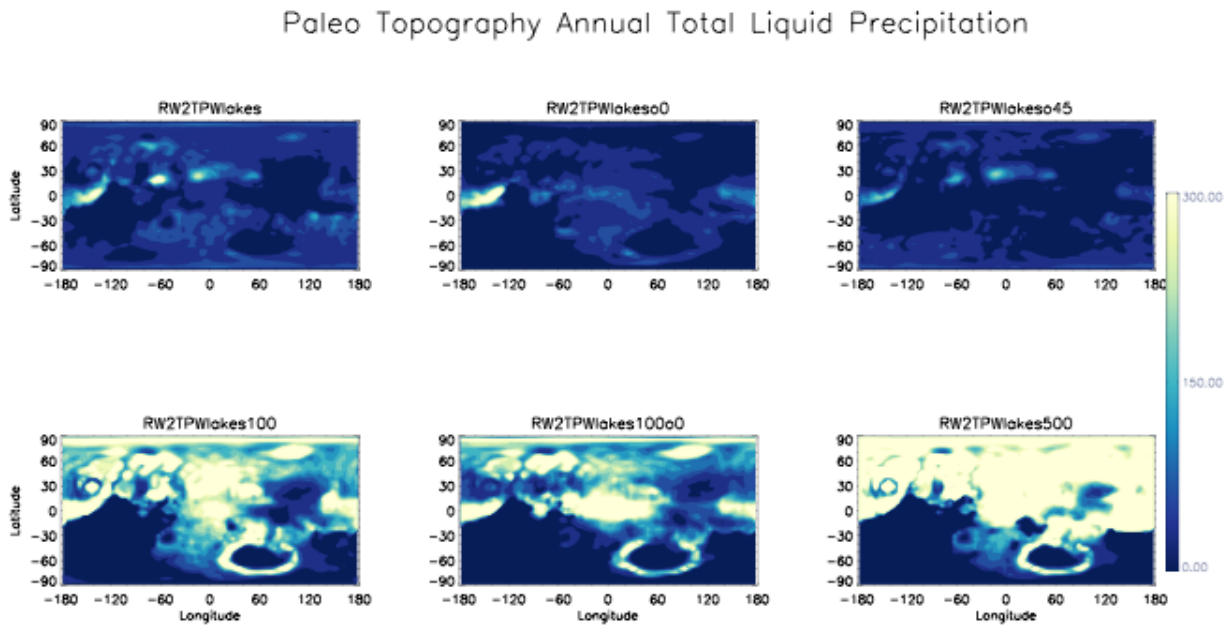

Figure 15. Same as Figure 14 except for annual total liquid precipitation (mm).

Figure 15 shows that the planet is strongly divided between locations with predominant snowfall and those with predominant rainfall in the paleotopography simulations. Comparing Figure 15 to Figure 13 shows that areas with annual mean temperatures below freezing see very little or no rainfall. Much of the rainfall occurs in the northern hemisphere in all the simulations, but there is rainfall in the southern hemisphere low latitudes, particularly from 60°W to 180°E. This partially overlaps the expected region of the valley network formations if they formed prior to Tharsis and associated true polar wander [Bouley et al., 2016], but the western portion of this region does not have any significant rainfall in any of our simulations. Using the paleotopography, the simulations with either 0° or modern (25.19°) obliquity produce rainfall in this latitude band, with slightly more rainfall in the simulations with modern obliquity. Again, 45° obliquity is not consistent with rainfall over locations with valley network formations.

3.2. Ocean Simulations

Our final set of simulations uses ROCKE-3D's fully coupled dynamic ocean capability. Most other published ancient Mars ocean simulations used mixed layer oceans (e.g., Kamada et al. (2020)). All previously discussed simulations with surface liquid water use dynamic lakes that form or evaporate based on precipitation patterns. In these simulations, water is initialized in oceans. We began a wide spectrum of such simulations, but the majority did not reach radiative and hydrological equilibrium before a shallow point of the ocean froze across the full depth. This freezing crashes the model and ends the simulation. Two ocean simulations did reach equilibrium, all using modern topography and obliquity values. Following a long history of research discussing the possibility of an ancient martian northern hemisphere ocean (e.g., Di Achille and Hynek, 2010), we simulate such a northern ocean. Additionally, since Hellas basin is the lowest topographic point on the planet, we conduct a simulation with a Hellas ocean. Here we introduce the impacts of these oceans on the broader planetary climate and reserve more in-depth analysis (hopefully with additional successful simulations) to future work.

Figure 16 provides an initial orientation to our two simulations with fully coupled dynamic oceans. The northern hemisphere ocean fills the northern lowlands Arcadia, Acidalia, and Utopia Planitae to the -3900 m isohypse, whereas the Hellas ocean fills much of that basin to the same level. The bottom two panels of Figure 16 should look quite similar to those of the bottom middle two panels of Figure 5 since they use the same atmospheric gas composition. The subtle differences relate to the moderating influence of the oceans. The ocean basins are cooler than equivalent land surfaces in comparable simulations.

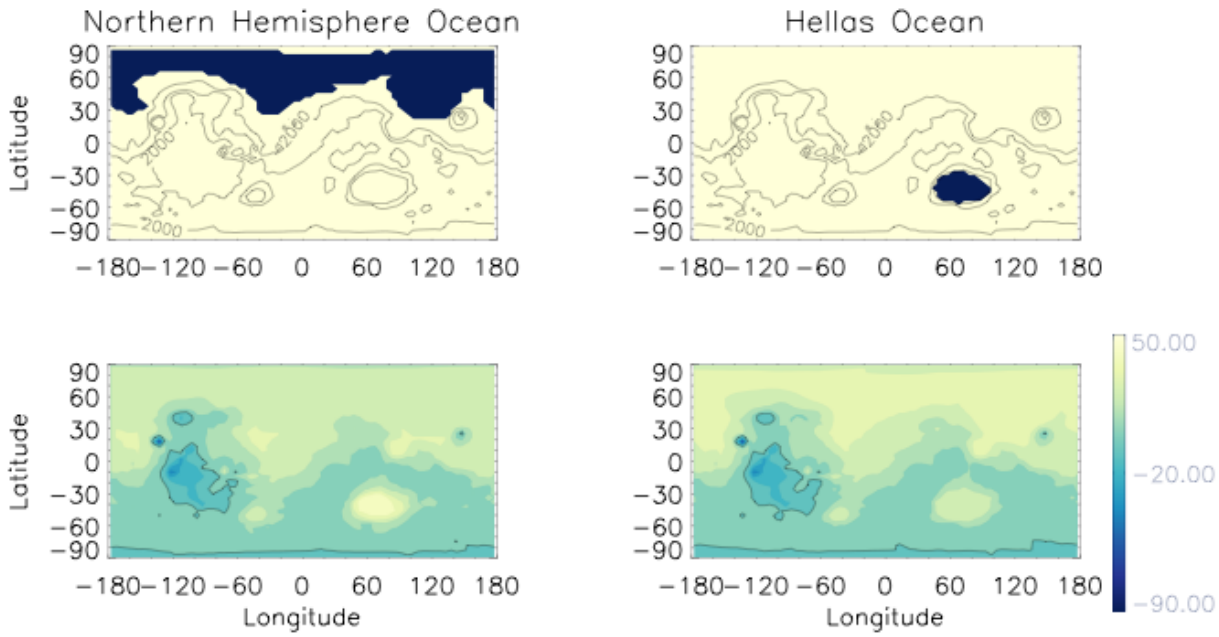

Figure 16. The location of the northern hemisphere ocean and Hellas ocean (dark fill) and planetary topography (lines contoured at -2000, 0, and 2000 m; top row). The annual average surface temperatures for those two simulations (°C; bottom row).

Our goal for the ocean simulations was to see if the abilities of oceans to alter planetary climates through ocean heat transport, their great thermal inertia, and changing atmospheric flows and precipitation patterns could be manifested in a way that would make a temperate Noachian climate on Mars more durable. In other words, would the creation of a Noachian ocean on Mars help stabilize and warm the climate in a way that would help perpetuate that temperature climate for a longer duration than might otherwise be true? To diagnose this, we compare our two ocean simulations with the RW2lakes simulation. The ocean simulations have identical atmospheric pressure and gas compositions to the RW2lakes simulation as well as using modern topography and obliquity. As noted earlier, when using modern topography, the initial water inventory of the planet did not alter the final stable end climactic state, so no significant difference would be found in comparing the ocean simulations to the RW2lakes500 (with 500 m GEL water), for example.

571 Figure 17 demonstrates how the two ocean configurations alter the simulated climate. As
572 seen in the top row, there is very little difference (<1°C) in annual average surface temperature for
573 most of the planet if an ocean is present. Only the ocean itself, which is notably cooler than open
574 dry ground, produces a change to annual average temperatures. This alone answers one of our
575 questions regarding the influence of an ancient ocean on Noachian martian climate. Both a
576 northern hemisphere or Hellas ocean are inefficiently distributed to allow substantial meridional
577 heat transport which could help warm the planet and redistribute energy through the climate
578 system. Hence, there is a marginal effect on planetary surface temperature. Note however, that a
579 2 bar martian atmosphere does have very efficient *atmospheric* meridional heat transport due to
580 the greater mass per unit area relative to Earth. The effect of atmospheric density on heat transport
581 is discussed in the context of tidally-locked planets around M-stars by, e.g., Joshi et al. (1997) and
582 Wordsworth (2015).

583 There is however a notable change in precipitation patterns around the planet. This is
584 expected due to the larger surface liquid water inventory allowing increased evaporation and more
585 available liquid water in the climate system. Recall that one key finding of the simulations with
586 surface liquid water initialized in active lakes is that water is cold-trapped on Tharsis. The ocean
587 simulations do produce widespread snow and ice cover on Tharsis, as did those with active lakes,
588 but the simulation can not evaporate the ocean and redeposit it as snow on Tharsis as may happen
589 over geologic time in such a situation. These ocean simulations are hydrologically equilibrated,
590 but it is reasonable to assume that ocean depth would drop slowly through time as water is
591 deposited at the south pole and Tharsis. Indeed, as shown in Figure 17, precipitation near Tharsis
592 is increased in these simulations, particularly for the northern hemisphere ocean simulation (to be
593 expected given the proximity of the ocean to the Tharsis highlands). The Hellas ocean sees

increased precipitation throughout the southern hemisphere, while the greatest change for the northern hemisphere ocean simulation is over that ocean itself.

Most notably, rainfall increases throughout the southern hemisphere and along the dichotomy boundary, including over many locations with valley network formations, with the Hellas ocean simulation. In the northern hemisphere ocean simulation, there is also a modest increase of rainfall along the dichotomy boundary (particularly from 60-150°E). There is also much more rainfall near Elysium Mons (25°N, 140°W).

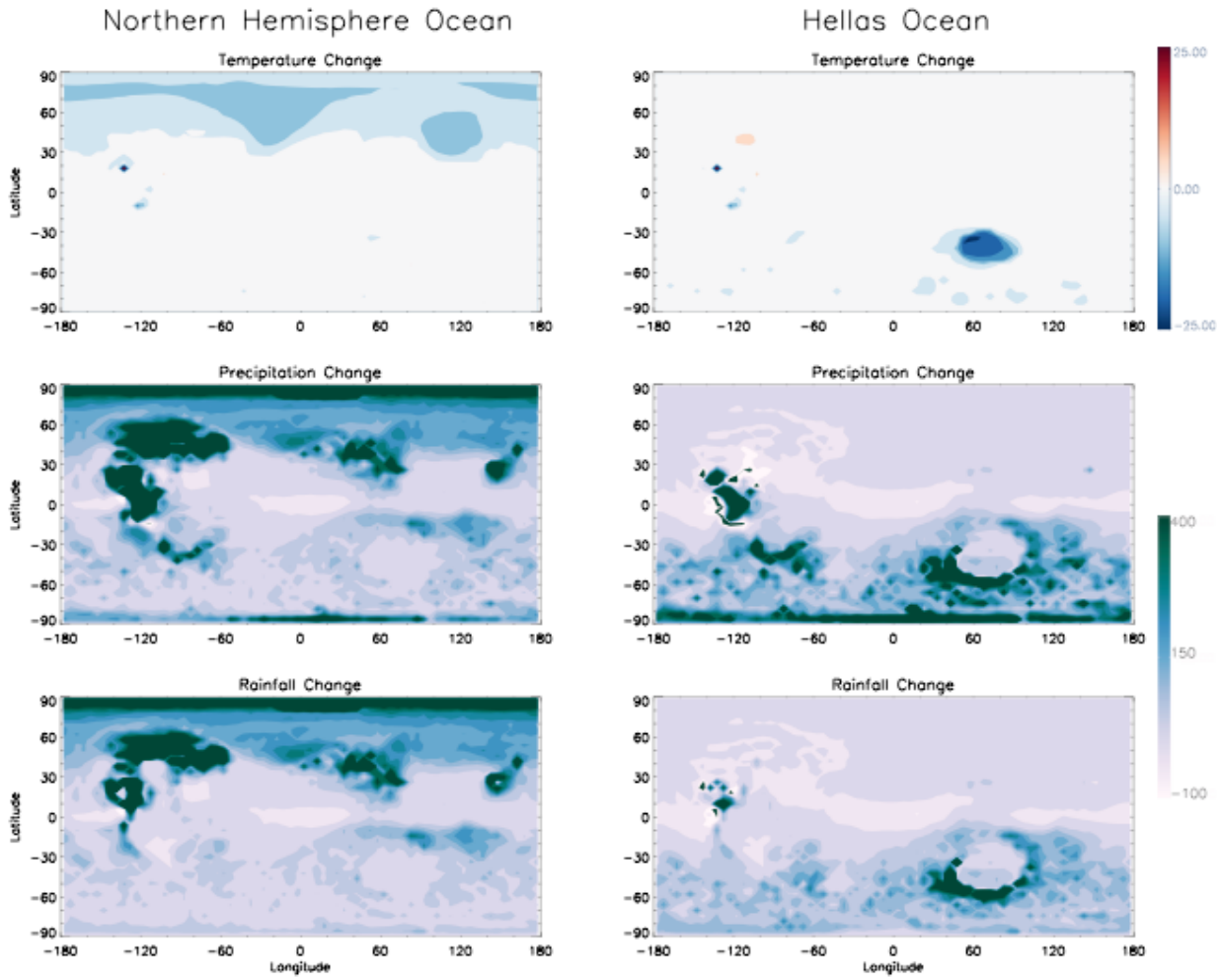

Figure 17. Change in annual average surface temperature (°C, top row), change in annual precipitation (mm, middle row), and chance in annual rainfall (mm, bottom row) when comparing the RW2lakes simulation to the northern hemisphere ocean simulation (left column) and Hellas ocean simulation (right column).

4. CONCLUSIONS

In this work we sought to test whether the climate on Noachian Mars could have maintained "warm and wet" conditions with reasonable constraints on surface air pressure (2 bar or less) and the possible availability of H_2-CO_2 collision-induced absorption using ROCKE-3D, a capable and flexible GCM. With ROCKE-3D, the answer to this question is "yes." CO_2-dominated atmospheres with surface pressures above ~1.5 bar and H_2 mixing ratios of ≥3% produce global mean surface temperatures above the freezing point of water. Our work is agnostic to the source of the H_2 and its duration in the atmosphere.

Note however, that in these initial simulations without significant amounts of water (indeed, with a global water inventory more akin to modern Mars), the warmest locations are in the northern hemisphere lowlands and Hellas basins. These are both locations far removed from the places with geologic evidence of past fluvial activity in the southern hemisphere highlands near the topographic dichotomy boundary and elsewhere. Much of the southern hemisphere and Tharsis region have annual average temperatures well below freezing.

Additionally, some of our tested atmospheric gas mixtures included CH_4. We found that a small amount of CH_4, 1% in our simulations, could have had important implications for ancient water loss on Mars. Simulations that included CH_4 produce a weak and leaky stratosphere, where warming temperatures limit water cloud formation, but where the upper tropospheric cold trap is insufficient to limit vertical transport of water into the stratosphere where it could be photodissociated and lost to space. Simulations without CH_4 have thicker water clouds in the upper troposphere that acts as a more efficient hygropause, reducing water flux into the upper atmosphere. Future work should address the implications of CH_4 and water ice clouds on water loss from Noachian Mars in more detail.

631 After finding an atmospheric gas mixture that produced global mean temperatures above
632 freezing (RW2 = 94% CO_2, 5% H_2, and 1% CH_4 following Wordsworth et al. [2017]), our second
633 set of simulations looked at the hydrological cycle of the planet under these possible warm and
634 wet conditions. Using modern topography, the vast majority of water on the planet, regardless of
635 the initial water inventory, is cold-trapped on the high and frigid Tharsis plateau. ROCKE-3D
636 does not have a land ice or glacier parameterization that could simulate the eventual flow of these
637 glaciers and determine how glacial melt could recharge the system. But regardless, the planet is
638 left with comparatively little water in the active hydrological cycle. We find planetary obliquity
639 is key to determining where precipitation falls as rain or snow in these simulations. Simulations
640 with 0° obliquity produce greater rainfall near locations with valley network formations.
641 Simulations with 45° obliquity are slightly cooler than those with either modern or 0° obliquity
642 and have rainfall patterns that are inconsistent with the geologic evidence for fluvial activity on
643 Noachian Mars. Note our simulations do not include the physics of CO_2 condensation. But
644 importantly, many of our simulations that included H_2 had surface temperatures remain above the
645 CO_2 condensation temperature, regardless of obliquity.
646 The timing of the formation of Tharsis relative to the valley network formations is critical
647 to understanding the climatic conditions under which they formed. Simulations using a plausible
648 paleotopography (see Bouley et al. [2016]) have increased amounts of precipitation globally due
649 to the lack of Tharsis acting as a cold trap for snow and ice. Again, simulations with modern or
650 0° obliquity are more consistent with rainfall over locations with valley network formations than
651 45° obliquity.
652 If Noachian Mars had oceans (following Tharsis emplacement with modern topography),
653 the most plausible locations for those oceans in the northern hemisphere lowlands and Hellas basin

654 are inefficient for meridional heat transport. The global climate is no warmer when an ocean is
655 present than when it is absent, assuming the background atmospheric composition is supportive of
656 surface liquid water already. The presence of oceans does alter precipitation patterns, however,
657 and precipitation and rainfall are increased over much of the planet. A Hellas ocean in particular
658 produces increased rainfall in many locations where valley network formations and paleolakes are
659 seen in the modern surface geology.
660
661 ACKNOWLEDGEMENTS
662 Guzewich, Way, Del Genio, Aleinov, Wolf, and Tsigaridis were supported by the NASA Nexus
663 for Exoplanet System Science program that helped develop the ROCKE-3D GCM. We thank
664 Bouley et al. (2016) for helpfully including the paleotopographic file in their supplemental material
665 to make some of these simulations plausible. Model input and boundary condition files, rundecks
666 (simulation setup files), and final output files are available here: .
667
668 REFERENCES
669
670 Abramopoulos, F., Rosenzweig, C., & Choudhury, B. (1988). Improved Ground Hydrology
671 Calculations for Global Climate Models (GCMs): Soil Water Movement and Evapotranspiration,
672 Journal of Climate, 1(9), 921-941. doi:10.1175/1520-0442(1988)001<0921:IGHCFG>2.0.CO;2
673
674 Batalha, N., S.D. Domagal-Goldman, R. Ramirez and J.F. Kasting (2015), Testing the early
675 Mars H2–CO2 greenhouse hypothesis with a 1-D photochemical model, Icarus, 258, 337-349,
676 https://doi.org/10.1016/j.icarus.2015.06.016.
677
678 Bouley, S., Baratoux, D., Matsuyama, I. *et al* (2016). Late Tharsis formation and implications for
679 early Mars, *Nature* 531, 344–34, https://doi.org/10.1038/nature17171.
680
681 Bouley, S., Baratoux, D., Paulien, N., Missenard, Y., Saint-Bézar, B. (2017), The revised
682 tectonic history of Tharsis, Earth and Planetary Science Letters, 488, 126-133,
683 https://doi.org/10.1016/j.epsl.2018.02.019.

Bryne, B., and C. Goldblatt (2015), Diminished greenhouse warming from Archean methane due to solar absorption lines, Climate of the Past, 11, 559-570, doi:10.5194/cp-11-559-2015.

Cassata, W., D.L. Schuster, P.R. Renne, and B.P. Weiss (2012), Trapped Ar isotopes in meteorite ALH 84001 indicate Mars did not have a thick ancient atmosphere. *Icarus,* 221, 461–465, https://doi.org/10.1016/j.icarus.2012.05.005.

Carr, M. H. (1996), *Water on Mars*, 229 pp., Oxford Univ. Press, New York.

Carter, J., Poulet, F., Bibring, J.-P., Mangold, N., and Murchie, S. (2013), Hydrous minerals on Mars as seen by the CRISM and OMEGA imaging spectrometers: Updated global view, *J. Geophys. Res. Planets*, 118, 831– 858, doi: 10.1029/2012JE004145.

Cassanelli JP, Head JW III (2015), Firn densification in a Late Noachian "icy highlands" Mars: implications for ice sheet evolution and thermal response, *Icarus* 253:243–55, https://doi.org/10.1016/j.icarus.2015.03.004.

Claire, M.W., Sheets, J., Cohen, M., Ribas, I., Meadows, V.S., & Catling, D. (2012) "The Evolution of Solar Flux From 0.1 nm to 160 μm: Quantitative Estimates for Planetary Studies." *The Astrophysical Journal* 757:95 (12pp)

Clancy, R., A. W. Grossman, M. J. Wolff, P. B. James, D. J. Rudy, Y. N. Billawala, B. J. Sandor, S. W. Lee, and D. O. Muhleman(1996), Water vapor saturation at low altitudes around Mars aphelion: A key to Mars climate, *Icarus*, 122, 36–62, https://doi.org/10.1006/icar.1996.0108.

Clough, S. A., Shephard, M. W., Mlawer, E. J., Delamre, J. S., Iacono, M. J., Cady-Pereira, K., Boukabara, S., and Brown, P. D. (2005), Atmospheric radiative trasnfer modeling: a summary of the AER codes. *J. Quant. Spec. Rad. Trans.* 91, 233-244. doi:10.1016/j.jqsrt.2004.05.058

Di Achille, G. and B.M. Hynek (2010), Ancient ocean on Mars supported by global distribution of deltas and valleys, Nature Geoscience, 3, 459–463, https://doi.org/10.1038/ngeo891.

Ehlmann, B., Mustard, J., Murchie, S. *et al.* Subsurface water and clay mineral formation during the early history of Mars. *Nature* 479, 53–60 (2011). https://doi.org/10.1038/nature10582.

Fassett, C. I., and Head, J. W. (2005), Fluvial sedimentary deposits on Mars: Ancient deltas in a crater lake in the Nili Fossae region, *Geophys. Res. Lett.*, 32, L14201, doi:10.1029/2005GL023456.

724 Fastook JL, Head JW III, Marchant DR, Forget F, Madeleine JB (2012), Early Mars climate near
725 the Noachian–Hesperian boundary: independent evidence for cold conditions from basal melting
726 of the south polar ice sheet (Dorsa Argentea formation) and implications for valley network
727 formation. *Icarus* 219:25–40, https://doi.org/10.1016/j.icarus.2012.02.013.
728
729 Fastook JL, Head JW III (2014), Glaciation in the Late Noachian icy highlands: ice
730 accumulation, distribution, flow rates, basal melting, and top-down melting rates and
731 patterns,*Planet. Space Sci.* 106:82–98, https://doi.org/10.1016/j.pss.2014.11.028.
732
733 Forget, F., and R. Pierrehumbert (1997), Warming Early Mars with Carbon Dioxide Clouds That
734 Scatter Infrared Radiation, Science, 278, 5341, 1273-1276, DOI:
735 10.1126/science.278.5341.1273.
736
737 Forget, F., et al. (2013), 3D modelling of the early martian climate under a denser CO2
738 atmosphere: Temperatures and CO_2 ice clouds, Icarus, 222(1), 81-99,
739 https://doi.org/10.1016/j.icarus.2012.10.019.
740
741 Godin, P. J., Ramirez, R. M., Campbell, C. L., Wizenberg, T., Nguyen, T. G., Strong, K. and
742 Moores, J. E. (2020) Collision-Induced Absorption of CH_4-CO_2 and H_2-CO_2 Complexes and
743 Their Effect on the Ancient Martian Atmosphere. *J. Geophys. Res. Planets.*, 125, 12,
744 e2019JE006357. https://doi.org/10.1029/2019JE006357
745
746 Gough, D.O. (1981) "Solar Interior Structure and Luminosity Variations." *Solar Physics* 74, 21-
747 34
748
749 Grant, J. A., Wilson, S. A., Mangold, N., Calef, F., and Grotzinger, J. P. (2014), The timing of
750 alluvial activity in Gale crater, Mars, *Geophys. Res. Lett.*, 41, 1142– 1148,
751 doi:10.1002/2013GL058909.
752
753 Grotzinger, J.P. et al., (2014), A Habitable Fluvio-Lacustrine Environment at Yellowknife Bay,
754 Gale Crater, Mars, Science, 343, 6169, DOI: 10.1126/science.1242777.
755
756 Haberle, R. M., Zahnle, K., Barlow, N. G., & Steakley, K. E. (2019). Impact degassing of H2
757 on early mars and its effect on the climate system. *Geophysical Research Letters*, 46, 13355–
758 13362. https://doi.org/10.1029/2019GL084733.
759
760 Hansen, J., G. Russell, D. Rind, P. Stone, A. Lacis, S. Lebedeff, R. Ruedy, and L. Travis, 1983:
761 Efficient three-dimensional global models for climate studies: Models I and II. Mon. Weather
762 Rev., 111, 609-662, doi:10.1175/1520-0493(1983)111<0609:ETDGMF>2.0.CO;2.
763

764 Hayworth, B.P.C., R.K. Kopparapu, J. Haqq-Misra et al. (2020), Warming early Mars with
765 climate cycling: The effect of CO_2-H_2 collision-induced absorption, *Icarus*, 345,
766 https://doi.org/10.1016/j.icarus.2020.113770.
767
768 Hirschmann MM, Withers AC. (2008), Ventilation of CO2 from a reduced mantle and
769 consequences for the early Martian greenhouse, *Earth Planet. Sci. Lett.* 270:147–55,
770 https://doi.org/10.1016/j.epsl.2008.03.034.
771
772 Hurowitz, J.A., Fischer, W.W., Tosca, N.J. and Milliken, R.E., 2010. Origin of acidic surface
773 waters and the evolution of atmospheric chemistry on early Mars. Nature Geoscience, 3(5),
774 pp.323-326.
775
776 Hynek, B.M. and R.J. Phillips (2001), Evidence for Extensive Denudation of the Martian
777 Highlands, Geology, 21(5), 407-410, https://doi.org/10.1130/0091-
778 7613(2001)029<0407:EFEDOT>2.0.CO;2.
779
780 Hynek, B. M., Beach, M., and Hoke, M. R. T. (2010), Updated global map of Martian valley
781 networks and implications for climate and hydrologic processes, *J. Geophys. Res.*, 115, E09008,
782 doi:10.1029/2009JE003548.
783
784 Irwin, R. P., Howard, A. D., Craddock, R. A., and Moore, J. M. (2005), An intense terminal
785 epoch of widespread fluvial activity on early Mars: 2. Increased runoff and paleolake
786 development, *J. Geophys. Res.*, 110, E12S15, doi:10.1029/2005JE002460.
787
788 Jakosky, B.M. et al. (2018), Loss of the Martian atmosphere to space: Present-day loss rates
789 determined from MAVEN observations and integrated loss through time, Icarus, 315, 146-157,
790 doi: 10.1016/j.icarus.2018.05.030.
791
792 Kamada, A., T. Kuroda, Y. Kasaba, N. Terada, H. Nakagawa, and K. Toriumi (2020), A coupled
793 atmosphere-hydrosphere climate model of early Mars: A 'cool and wet' scenario for the
794 formation of water channels, Icarus, 338, 113567, https://doi.org/10.1016/j.icarus.2019.113567.
795
796 Kasting, J.F. (1991), CO2 Condensation and the Climate of Early Mars, Icarus, 94(1), 1-13,
797 https://doi.org/10.1016/0019-1035(91)90137-I.
798
799 Kasting, J.F. (1997), Warming Early Earth and Mars, Science, 279, 5316, DOI:
800 10.1126/science.276.5316.1213.
801
802 Kerber, L., F. Forget, and R.D. Wordsworth (20150, Sulfur in the early martian atmosphere
803 revisited: Experiments with a 3-D Global Climate Model, Icarus, 261, 133-148,
804 https://doi.org/10.1016/j.icarus.2015.08.011.

Kite, E. S., Williams, J.-P., Lucas, A., & Aharonson, O. (2014). Low palaeopressure of the martian atmosphere estimated from the size distribution of ancient craters. *Nature Geoscience*, 7, 335–339, https://doi.org/10.1038/ngeo2137.

Kite, E. S., Sneed, J., Mayer, D. P., and Wilson, S. A. (2017), Persistent or repeated surface habitability on Mars during the late Hesperian - Amazonian, *Geophys. Res. Lett.*, 44, 3991–3999, doi:10.1002/2017GL072660.

Kopparapu, R. K., Ramirez, R., Kasting, J.F., Eymet, V., Robinson, T.D., Mahadevan, S., Terrien, R.C., Domagal-Goldman, S., Meadows, V., and Deshpande, R. (2013) "Habitable Zones Around Main-Sequence Stars: New Estimates." *The Astrophysical Journal* 765:131(16pp)

Kuhn, W. R., and S. K. Atreya, Ammonia photolysis and the greenhouse effect in the primordial atmosphere of the Earth, Icarus, 37, 207-213, 1979, https://doi.org/10.1016/0019-1035(79)90126-X.

Lean, J., Beer, J. and Bradley, S. (1995) "Reconstruction of solar irradiance since 1610: Implications for climate change." *Geophys. Res. Lett.* 22, 3195-3198

Manga, M., Patel, A., Dufek, J., and Kite, E. S. (2012), Wet surface and dense atmosphere on early Mars suggested by the bomb sag at Home Plate, Mars, *Geophys. Res. Lett.*, 39, L01202, doi:10.1029/2011GL050192.

Matsuyama, I. & Manga, M. (2010), Mars without the equilibrium rotational figure, Tharsis, and the remnant rotational figure. *J. Geophys. Res.* 115, E12020.

Masursky, H. (1973), An overview of geological results from Mariner 9, *J. Geophys. Res.*, 78(20), 4009– 4030, doi:10.1029/JB078i020p04009.

Mischna, M. A., Baker, V., Milliken, R., Richardson, M., and Lee, C. (2013), Effects of obliquity and water vapor/trace gas greenhouses in the early martian climate, *J. Geophys. Res. Planets*, 118, 560– 576, doi:10.1002/jgre.20054.

Murchie, S., et al. (2009), Evidence for the origin of layered deposits in Candor Chasma, Mars, from mineral composition and hydrologic modeling, *J. Geophys. Res.*, 114, E00D05, doi:10.1029/2009JE003343.

Mondelain, D., C. Boulet, and J.-M. Hartmann (2021), The binary absorption coefficients for H2 + CO2mixtures in the 2.12–2.35 μm spectral region determined by CRDS and by semi-empirical

calculations, Journal of Quantitative Spectroscopy and Radiative Transfer, 260, 107454, https://doi.org/10.1016/j.jqsrt.2020.107454.

Navarro, T., Madeleine, J.-B, Forget, F., Spiga, A., Millour, E., Montmessin, F., and Määttänen, A. (2014), Global climate modeling of the Martian water cycle with improved microphysics and radiatively active water ice clouds, *J. Geophys. Res. Planets*, 119, 1479– 1495, doi:10.1002/2013JE004550.

Palumbo, A. M., & Head, J. W. (2018). Early Mars climate history: Characterizing a "warm and wet" Martian climate with a 3-D global climate model and testing geological predictions. *Geophysical Research Letters*, 45, 10,249– 10,258. https://doi.org/10.1029/2018GL079767.

Palumbo, A.M., J.W. Head, and L. Wilson (2020), Rainfall on Noachian Mars: Nature, timing, and influence on geologic processes and climate history, Icarus, 347, 113782, https://doi.org/10.1016/j.icarus.2020.113782.

Perron, J. T., Mitrovica, J. X., Manga, M., Matsuyama, I. & Richards, M. A., (2007) Evidence for an ancient martian ocean in the topography of deformed shorelines. *Nature,* 447, 840–843.

Pieri, D.C. (1981), Martian Valleys: Morphology, Distribution, Age, and Origin, Science, 210, 4472, 895-897, DOI: 10.1126/science.210.4472.895.

Pollack, J.B. (1979), Climate Change on the Terrestrial Planets, Icarus, 37, 479-553, https://doi.org/10.1016/0019-1035(79)90012-5.

Pollack, J. B., J. F. Kasting, S. M. Richardson, and K. Poliakoff (1987), The case for a wet, warm climate on early Mars, Icarus 71, 203-224, https://doi.org/10.1016/0019-1035(87)90147-3.

Postawko, S. E., and Kuhn, W. R. (1986), Effect of the greenhouse gases (CO2, H2O, SO2) on Martian paleoclimate, *J. Geophys. Res.*, 91(B4), 431– 438, doi:10.1029/JB091iB04p0D431.

Ramirez, R., Kopparapu, R., Zugger, M. *et al.* Warming early Mars with CO2 and H2.*Nature Geosci* 7, 59–63 (2014). https://doi.org/10.1038/ngeo2000.

Ramirez, R.M., Craddock, R.A., and Usui, T. (2020), Climate Simulations for Early Mars with Estimated Precipitation, Runoff, and Erosion Rates, *J. Geophys. Res. Planets,* 125, e2019JE006160, https://doi.org/10.1029/2019JE006160.

Roe, H.G., (2012), Titan's Methane Weather, Annual Review of Earth and Planetary Science, 40:355-82, doi:10.1146/annurev-earth-040809-152548.

884 Rosenzweig, C., & Abramopoulos, F. (1997). Land-Surface Model Development for the GISS
885 GCM, Journal of Climate, 10(8), 2040-2054. doi:10.1175/1520-
886 0442(1997)010<2040:LSMDFT>2.0.CO;2
887
888 Schon, S. C., J. W. Head, and C. I. Fassett (2012), An overfilled lacustrine system and
889 progradational delta in Jezero crater, Mars: Implications for Noachian climate, Planet. Space
890 Sci., 67, 28–45, doi:10.1016/j.pss.2012.02.003.
891
892 Soto, A., M. I. Richardson, and C. E. Newman (2010), Global constraints on rainfall on ancient
893 Mars: Oceans, lakes, and valley networks, *Lunar Planet. Sci.*, *, XLI*, Abstract 2397.
894
895 Tarnas, J.D., Mustard, J.F., Lollar, B.S., Bramble, M.S., Cannon, K.M., Palumbo, A.M. and
896 Plesa, A.C., 2018. Radiolytic H2 production on Noachian Mars: Implications for habitability and
897 atmospheric warming. Earth and Planetary Science Letters, 502, pp.133-145.
898 Tian F, Claire MW, Haqq-Misra JD, Smith M, Crisp DC, et al. (2010), Photochemical and
899 climate consequences of sulfur outgassing on early Mars. Earth Planet. Sci. Lett. 295: 412–18,
900 https://doi.org/10.1016/j.epsl.2010.04.016.
901
902 Tosca, N.J., Ahmed, I.A., Tutolo, B.M., Ashpitel, A. and Hurowitz, J.A., 2018. Magnetite
903 authigenesis and the warming of early Mars. Nature geoscience, 11(9), pp.635-639.
904
905 Turbet, M., Gillmann, C., Forget, F., Baudin, B., Palumbo, A., Head, J. and Karatekin, O. (2020)
906 The environmental effects of very larger bolide impacts on early Mars explored with a hierarchy
907 of numerical models. *Icarus*, 335, 113419. https://doi.org/10.1016/j.icarus.2019.113419
908
909 Turbet, M., C. Boulet, and T. Karman (2020b), Measurements and semi-empirical calculations of
910 CO2 + CH4 and CO2 + H2 collision-induced absorption across a wide range of wavelengths and
911 temperatures. Application for the prediction of early Mars surface temperature, Icarus, in press,
912 https://doi.org/10.1016/j.icarus.2020.113762
913
914 Urata, R. A. and Toon, O. B. (2013), Simulations of the martian hydrologic cycle with a general
915 circulation model: Implications for the ancient martian climate, *Icarus*, 226, 229-250.
916 http://dx.doi.org/10.1016/j.icarus.2013.05.014
917
918 Warren, A. O., Kite, E. S., Williams, J.-P., & Horgan, B. (2019). Through the thick and thin:
919 New constraints on Mars paleopressure history 3.8 - 4 Ga from small exhumed craters. *Journal
920 of Geophysical Research: Planets*, 124, 2793– 2818. https://doi.org/10.1029/2019JE006178.
921
922 Way, M.J., A.D. Del Genio, N.Y. Kiang, L.E. Sohl, D.H. Grinspoon, I. Aleinov, M. Kelley, and
923 T. Clune, 2016: Was Venus the first habitable world of our solar system? *Geophys. Res. Lett.*,
924 **43**, no. 16, 8376-8383, doi:10.1002/2016GL069790.

Way, M.J., I. Aleinov, D.S. Amundsen, M.A. Chandler, T. Clune, A.D. Del Genio, Y. Fujii, M. Kelley, N.Y. Kiang, L. Sohl, and K. Tsigaridis, 2017: Resolving Orbital and Climate Keys of Earth and Extraterrestrial Environments with Dynamics 1.0: A general circulation model for simulating the climates of rocky planets. *Astrophys. J. Supp. Series*, **231**, no. 1, 12, doi:10.3847/1538-4365/aa7a06.

Way, M.J., A.D. Del Genio, I., Aleinov, T.L., Clune, M. Kelley, N.Y. Kiang, 2018: Climates of Warm Earth-like Planets I 3D Model Simulations. Astrophys. J. Supp. Series, 239, 24 doi:10.3847/1538-4365/aae9e1

Way, M.J., and A.D. Del Genio, 2020: Venusian habitable climate scenarios: Modeling Venus through time and applications to slowly rotating Venus-like exoplanets. J. Geophys. Res,: Planets, 125, e2019JE006276. doi:10.1029/2019JE006276

Williams, R.M.E. et al. (2013), Martian Fluvial Conglomerates at Gale Crater, Science, 340, 6136, 1068-1072, DOI: 10.1126/science.1237317.

Wolf, E. T. and Toon, O. B. (2013), Hospitable archean climates simulated by a general circulation model, Astrobiology, 13, 656–673, doi:10.1089/ast.2012.0936.

Wordsworth, R., Forget, F., and Eymet, V. (2010) "Infrared collision-induced and far-line absorption in dense CO_2 atmospheres." *Icarus* 210, 992-997

Wordsworth R, Pierrehumbert R (2013), Hydrogen-nitrogen greenhouse warming in Earth's early atmosphere. *Science* 339:64–67, DOI: 10.1126/science.1225759.

Wordsworth R, Forget F, Millour E, Head JW, Madeleine JB, Charnay B. (2013), Global modelling of the early martian climate under a denser CO2 atmosphere: water cycle and ice evolution, *Icarus* 222:1–19, https://doi.org/10.1016/j.icarus.2012.09.036.

Wordsworth, R. (2015), Atmospheric heat redistribution and collapse on tidally locked rocky planets. The Astrophysical Journal, 806(2), p.180.

Wordsworth, R. D., Kerber, L., Pierrehumbert, R. T., Forget, F., and Head, J. W. (2015), Comparison of "warm and wet" and "cold and icy" scenarios for early Mars in a 3-D climate model, *J. Geophys. Res. Planets*, 120, 1201– 1219. doi:10.1002/2015JE004787.

Wordsworth, R.D. (2016), The Climate of Early Mars, Annual Review of Earth and Planetary Science, 44, 381-408, https://doi.org/10.1146/annurev-earth-060115-012355.

966 Wordsworth, R.D., Kalugina, Y., Lokshtanov, S., Vigasin, A., Ehlmann, B., Head, J.,
967 Sanders, C., and Wang, H. (2017), Transient reducing greenhouse warming on early Mars,
968 *Geophys. Res. Lett.*, 44, 665– 671, doi:10.1002/2016GL071766.
969
970 Yang, J., Leconte, J., Wolf, E.T., Goldblatt, C., Feldl, N., Merlis, T., Wang, Y, Koll, D.D.B.,
971 Ding, F., Forget, F. and Abbot, D.S. (2016) "Differences in Water Vapor Radiative Transfer
972 Among 1D Models Can Significantly Affect the Inner Edge of the Habitable Zone."
973 *The Astrophysical Journal*, 826:222 (11pp)
974
975
976
977
978